Titre: Title:	Experimental and Numerical Study of Needle Peening Effects in Aluminium Alloy 2024-T3 Sheets
Auteur: Author:	Julio Alberto Méndez Romero
Date:	2016
Type:	Mémoire ou thèse / Dissertation or Thesis
Référence: Citation:	Méndez Romero, J. A. (2016). Experimental and Numerical Study of Needle Peening Effects in Aluminium Alloy 2024-T3 Sheets [Mémoire de maîtrise, École Polytechnique de Montréal]. PolyPublie. https://publications.polymtl.ca/2062/

UNIVERSITÉ DE MONTRÉAL

EXPERIMENTAL AND NUMERICAL STUDY OF NEEDLE PEENING EFFECTS IN ALUMINIUM ALLOY 2024-T3 SHEETS

JULIO ALBERTO MÉNDEZ ROMERO
DÉPARTEMENT DE GÉNIE MÉCANIQUE
ÉCOLE POLYTECHNIQUE DE MONTRÉAL

MÉMOIRE PRÉSENTÉ EN VUE DE L'OBTENTION
DU DIPLÔME DE MAÎTRISE ÈS SCIENCES APPLIQUÉES
(GÉNIE MÉCANIQUE)
FÉVRIER 2016

UNIVERSITÉ DE MONTRÉAL

ÉCOLE POLYTECHNIQUE DE MONTRÉAL

Ce mémoire intitulé :

EXPERIMENTAL AND NUMERICAL STUDY OF NEEDLE PEENING EFFECTS IN ALUMINIUM ALLOY 2024-T3 SHEETS

présenté par : MÉNDEZ ROMERO Julio Alberto
en vue de l'obtention du diplôme de : Maîtrise ès sciences appliquées
a été dûment accepté par le jury d'examen constitué de:

M. VADEAN Aurelian, Doctorat, président
M. LÉVESQUE Martin, Ph. D., membre et directeur de recherche
M. GOSSELIN Frédérick, Doctorat, membre

DEDICATION

To my awesome family and friends
. . . You know I love you.

ACKNOWLEDGEMENTS

I would like to galantly express my gratitude to my research supervisor, Prof. Martin Lévesque for his supervision, guidance and expertise throughout this research as well as showing me the more human side of what the academic life compasses. I would also like to thank the jury members for their time, guidance and suggestions.

I would like to acknowledge Syvlain Forgues and Brigitte Labelle from Shockform Aeronautique Inc. for their support of this research by means of their experience, technology and infrastructure. I want to extend these thanks to the rest of their team who replied gladly to all of my questions and requests.

I wish to thank the members of the LM2 laboratory from École Polytechnique. Special thanks to Hongyan Miao, Fubin Tu, Alexandre Gariépy, and Pierre Faucheux for their helpful advice during my research activities. I would like to thank Stéphane Étienne and Cédric Béguin for providing the equipment used for the high-speed shooting. My special thanks go to Amrita Bag, Thierry Klotz and Charles Bianchetti for helping me in the transition into the research life.

And finally, I would like to thank my friends for supporting me and encouraging me. To my family, thanks for always being there - not only these last couple years but for showing their support in whatever endeavour I partake.

RÉSUMÉ

Le grenaillage est un procédé utilisé dans l'industrie aérospatiale pour améliorer la vie en fatigue des composantes soumises à des contraintes cycliques, comme les trains d'atterrissage, les voilures d'avoin et certaines pièces de moteurs. La méthode de grenaillage la plus commune consiste à projeter des petites billes sur la surface d'une pièce pour modifier sa structure de surface. Les impacts des billes, appelées grenailles, induisent des déformations plastiques en surface, ce qui conduit à des contraintes résiduelles compressives en surface. Bien que la grenailleuse soit utilisée pour le traitement de grandes pièces, il existe des technologies pour faire le grenaillage localisé, comme le grenaillage aux aiguilles. Ce travail de recherche a eu comme objectif d'analyser en détail le comportement d'un nouveau prototype d'appareil de grenaillage à aiguilles, appelé le SPIKER^{TM} pour en comprendre les effets sur les contraintes résiduelles de l'alliage AA2024-T3.

L'équipement a été premièrement caractérisé en utilisant une caméra à haute vitesse pour étudier son comportement en changeant la pression d'opération. L'ensemble des images collecté a été traité par un nouvel algorithme de manipulation numérique pour quantifier la vitesse et la fréquence des impacts des aiguilles. La vitesse au moment d'impact et la fréquence des impacts ont été déterminées pour différents paramètres d'opération. Il a été conclu que la vitesse et la fréquence des impacts augmentent avec la pression. Des anomalies du comportement, dont des variations de la fréquence et la vitesse parmi les aiguilles, ont été observées.

La réponse de l'alliage AA2024-T3 au grenaillage aux aiguilles a été étudiée expérimentalement sur des tôles d'une épaisseur de 1.6 mm. Les tôles ont été coupées aux dimensions des bandes Almen et traitées par le SPIKER®. L'alliage AA2024-T3 a été choisi car il a été bien étudié à l'École Polytechnique de Montréal dans la cadre de recherche de grenaillage conventionnel. Des essais de saturation ont été réalisés pour déterminer la déflection à la saturation pour plusieurs paramètres de grenaillage. La déflection a été aussi mesurée avec l'outil standard Almen utilisé dans la vérification périodique du traitement. Comme l'aluminium n'était pas magnétiquement compatible avec l'outil Almen, la déformation des échantillons a été mesurée avec une Machine à Mesurer Tridimensionnelle (MMT). La répétabilité du procédé a été démontrée et la déflection au point de saturation, comme le temps de saturation, ont été obtenus. Les diamètres des indentations crées par les impacts ont été mesurés pour les différentes valeurs de pression en utilisant la photographie microscopique. Il a été déterminé que la déformation des éprouvettes et les diamètres des indentations aug-

mentent avec la pression utilisée. Le traitement des échantillons avec les mêmes paramètres de grenaillage a créé des indentations de tailles variées. Cette observation est expliquée par la variation de la vitesse des impacts détectée pendant les essais de caractérisation. L'avantage que le grenaillage aux aiguilles fournit, en comparaison aux méthodes conventionnelles, est que l'uniformité des diamètres des indentations est plus facile à atteindre, car tous les impacts sont normaux, et de même énergie. Finalement la détermination des contraintes résiduelles a été effectuée par la Diffraction Rayons-X (DRX) pour un échantillon à saturation.

Un maillage éléments finis inspiré de travaux antérieurs à Polytechnique, a été développé pour simuler le grenaillage aux aiguilles. Les paramètres obtenus pendant les essaies de caractérisation ont été utilisés dans le modèle. La première partie de l'étude s'est intéressée à comparer les diamètres des cratères prédits et mesurés expérimentalement pour un seul impact. Une bonne adéquation a été observée.

Le modèle a été utilisé pour étudier le développement des contraintes résiduelles comme conséquence des impacts aléatoires à différentes vitesses. Le point de saturation a été déterminé en obtenant la déflection créée à partir des contraintes induites à partir de modèles developpés à Polytechnique. Le profil des contraints résiduelles au point de saturation pour un des cas a été comparé aux résultats obtenus par la DRX. Le modèle a été capable de prédire les contraintes résiduelles en surface (187 MPa) très proches de celles mesurées expérimentalement (184 MPa) . Finalement, la déflection prédite par le modèle a été comparée à celle mesurée expérimentalement pour différentes pressions d'opération. La différence maximale de déflection entre les résultats simulés et les résultats expérimentaux a été de 2% pour l'échantillon avec les contraintes résiduelles confirmées par la DRX. Une surestimation de 50% a été enregistrée pour la pression la plus faible, mais demeure entre 0.3% et le 13.2% pour les autres pressions. Comme conclusion, la méthodologie présentée prouve qu'il est possible de prédire les contraintes induites par le grenaillage aux aiguilles.

ABSTRACT

Peening of metallic components is an effective treatment used in aerospace and automotive applications to improve fatigue properties or to blend and repair localized damage. This process is typically carried out using metallic airborne media, called shot. However, different processes make use of different media, such is the case of hard, pneumatically powered needles of needle peening equipment. In order to obtain a better understanding of the effects of needle peening in the same context as shot peening, this research work had as an objective to study in detail the behavior of the needle peening equipment in order to characterize the process, design an experimental campaign to measure the effects of needle peening on AA2024-T3 and to develop and validate a Finite Element (FE) model capable of replicating the results of needle peening. The needle peening equipment prototype, called SPIKER®, was developed by Shockform Aeronautique Inc.

The equipment was characterized by utilizing high-speed camera recording in order to study its behaviour by varying the operating pressure. The obtained collection of images was ran through a newly developed digital image algorithm, so as to quantify the needles' velocity and frequency. The impact velocity and impact frequency were determined for different equipment operating parameters. It was concluded that both the average impact velocity and the impact frequency increase as the pressure becomes larger. Behaviour anomalies among the different needles, such as frequency and velocity variations, were brought to light; these conclusions could be of interest to the manufacturer. Ideally, all of the needles should behave as similarly as possible so as to produce a more uniform process.

The response to needle peening of AA2024-T3 in 1.6 mm thick sheet form was studied by needle peening test specimens with dimensions of an Almen strips using the SPIKER®. AA2024-T3 was selected since it was extensively studied at École Polytechnique de Montréal as part of previous shot peening research. Saturation tests were done to determine the deflection at saturation for different peening parameters. The specimen deflection was measured using the standard Almen gauge used as part of routinary process control. Due to the aluminium magnetic incompatibility with the Almen gauge, the deformed specimen profile was measured using a Coordinate Measuring Machine (CMM). Repeatability of the process was demonstrated and the deflection at saturation, as well as the saturation time, was obtained. The indentation diameters created by impacts for different operating pressures were measured using microscopic photography. It was determined that the specimen deformation, as well as the indentation diameter, is larger when the operating pressure increases. Treatment of the

test samples using the same peening parameters resulted in a variable indentation diameter. This is explained by the velocity variations detected during the equipment characterization. The added value that needle peening could provide to existing peening techniques is that, in principle, uniformity in the indentation diameters is easier to achieve as all impacts are normal and there is no loss of energy due to media interaction. The last experimental test was to determine the induced residual stress by means of X-ray Diffraction (XRD) for one specimen at saturation.

An FE model heavily inspired by previous shot peening modeling was developed to simulate needle peening. The parameters obtained during the characterization of the equipment were taken as boundary conditions. Initially, the case of a single impacts was studied. Good accordance between the simulated and the average experimental indentation diameters was obtained, except for the lowest pressure studied. The overestimation of the indentation diameter could stem from the method used to measure the simulated diameter. Coverage estimation, and therefore indentation diameters remain an open line of research in shot peening simulation. Using the same model, it was demonstrated that the induced stress profile changes in depth and magnitude as impact velocity increases.

Finally, the same model was used to study the development of residual stresses after multiple stochastic impacts at different velocities. Saturation was determined by obtaining the arc height created as as consequence of inducing the stresses determined by the impact model and obtaining a regression model that would best fit through the multiple simulation results. The residual stress profile at saturation for one of the scenarios was compared against the XRD results from the sample peened at the same operating pressure. The model was able to predict the surface residual stress (187 MPa) within 1.6% of the exprimental results (184 MPa). The results for the remainder of the cases studied were then compared against the deflection measured using the CMM. The maximum deflection difference between the predicted and the experimental results was of 2% for the sample for which the residual stress profile was confirmed. For the lowest air pressure, an overestimation of 50% was seen, however the difference between experimental and predicted results rests between 0.3% and 13.2% for the remainder of the cases. To conclude, the methodology presented proves that it is possible to predict the induced stresses by needle peening, which in hand can be used to predict sample deflection.

TABLE OF CONTENTS

DEDICATION iii

ACKNOWLEDGEMENTS iv

RÉSUMÉ v

ABSTRACT vii

TABLE OF CONTENTS ix

LIST OF TABLES xi

LIST OF FIGURES xii

LIST OF ACRONYMS xiv

LIST OF SYMBOLS xv

CHAPITRE 1 INTRODUCTION 1

INTRODUCTION 1
1.1 Introduction to needle peening 1
1.2 Problem definition 2
1.3 Thesis overview 3

CHAPITRE 2 LITERATURE REVIEW 4
2.1 Introduction to peening 4
2.2 Types of portable peening technologies 4
2.2.1 Shot peening 4
2.2.2 Rotary flap peening 5
2.2.3 Needle peening 6
2.3 Mechanics of peening 6
2.4 Process monitoring 6
2.4.1 Almen intensity 6
2.4.2 Surface coverage 8
2.5 Experimental studies on peening 8

2.5.1 Shot flow characterization 8
2.5.2 Residual stress 9
2.5.3 Material deformation 10
2.6 Analytical studies of peening results 11
2.6.1 Residual stresses 11
2.6.2 Material deformation and coverage 12
2.7 Numerical simulations of peening effects using the FE method 13
2.7.1 Dynamic impact models 13
2.7.2 Material constitutive theory 18
2.7.3 Peen forming 19

CHAPITRE 3 PROJECT RATIONALLE AND OBJECTIVES 21

CHAPITRE 4 RESEARCH METHODOLOGY 23
4.1 Needle peening application on AA2024 and process characterization 23
4.1.1 Equipment characterization 23
4.1.2 Experimental procedures 27
4.2 Numerical analysis 29
4.2.1 FE impact model 29
4.2.2 Specimen deflection 32

CHAPITRE 5 RESULTS 33
5.1 Needle peening application on AA2024 and process characterization 33
5.1.1 Equipment characterization 33
5.1.2 Experimental procedures 36
5.2 Numerical analysis 43
5.2.1 FE impact model - single impact 43
5.2.2 FE impact model - multiple impacts 47

CHAPITRE 6 GENERAL DISCUSSION 53

CHAPITRE 7 CONCLUSION 55

REFERENCES 57

LIST OF TABLES

Table 4.1	FE mesh geometry	30
Table 5.1	Relationship between peening pressure and measured arc height at saturation AH_s^m	40
Table 5.2	Relationship between air pressure and impact velocity	44
Table 5.3	Measured and predicted indentation diameters after single impact . .	45
Table 5.4	Arc height saturation solution for $v = 1.57$ mm/ms	48
Table 5.5	Predicted and measured arc height comparison	51

LIST OF FIGURES

Figure 1.1	Generation of indentations by needle peening	1
Figure 2.1	Typical induced stress profile after peening	5
Figure 2.2	Types of portable peening equipment	5
Figure 2.3	Processes of development of residual stresses	7
Figure 2.4	Process to determine the intensity of peening	8
Figure 2.5	Induced stresses by needle peening and shot peening in Ti6246	10
Figure 2.6	Schematic of the principle of stress forming	12
Figure 2.7	Meshing examples for two-dimensional models	15
Figure 2.8	Examples of three-dimensional FE models	15
Figure 2.9	Representative surface modeling proposed by Miao et al. (2009)	16
Figure 4.1	Simplified representation of the needle peening equipment prototype	23
Figure 4.2	High-speed camera recording set-up	24
Figure 4.3	Comparison of regression fit smoothening functions	26
Figure 4.4	Typical needle tip position as a function of time and computation of velocity at impact location	26
Figure 4.5	Test sample attached to an Almen holder and dimensions	28
Figure 4.6	Three-dimensional FE model	30
Figure 4.7	Unpeened areas in test specimen after needle peening	32
Figure 5.1	Individual needle velocities as a function of air pressure	33
Figure 5.2	Comparison between the dynamics of needles A and B; $p = 68.95$ kPa (10 psi)	34
Figure 5.3	Needle tip dynamics progression as a function of air pressure	34
Figure 5.4	Individual needle impact frequencies by air pressure	35
Figure 5.5	Saturation curve for $p = 137.89$ kPa (20 psi)	36
Figure 5.6	Saturation curves for $p = \{68.95, 103.42, 137.89, 172.37, 206.84\}$ kPa ($\{10, 15, 20, 25, 30\}$ psi) using Almen gauge values	37
Figure 5.7	Measuring path and CMM fixture diagram of test specimens	38
Figure 5.8	Specimen deflection profiles measured by CMM for $p = 137.89$ kPa (20 psi)	38
Figure 5.9	Arc height and saturation curve comparison between the deflection measurements using the Almen gauge and the CMM	39
Figure 5.10	Saturation curves for $p = \{68.95, 103.42, 137.89, 172.37, 206.84\}$ kPa ($\{10, 15, 20, 25, 30\}$ psi) using CMM values	40

Figure 5.11 Microscopic photography of indentations of test sample peened at $p =$ 137.89 kPa (20 psi) 41
Figure 5.12 Sampled indentation diameters and average size for $p = \{68.95, 103.42,$ $137.89, 172.37, 206.84\}$ kPa ($\{10, 15, 20, 25, 30\}$ psi) 42
Figure 5.13 Residual stresses σ_{res} profile on an AA2024-T3 strip peened at $p =$ 137.89 kPa (20 psi) 43
Figure 5.14 Convergence analysis between $R_n/10$ (Gariépy et al., 2011) and $R_n/15$ 44
Figure 5.15 Surface nodes U_Z after single impact for $v = 1.57$ mm/ms 45
Figure 5.16 Stresses in the X-direction measured under the impact point for $v =$ 1.57 mm/ms after a single impact 46
Figure 5.17 Cross-section induced stresses contour plot after single impact at various impact velocities 46
Figure 5.18 Average induced stress: $N = \{10, 20, 40, 80, 160, 320\}$, $v = 1.57$ mm/ms 48
Figure 5.19 Simulation calculation time: $N = \{10, 20, 40, 80, 160, 320\}$, $v = 1.57$ mm/ms 49
Figure 5.20 Simulated arc heights and fitted saturation curve for $v = 1.57$ mm/ms 49
Figure 5.21 Residual stress balancing for saturation of $v = 1.57$ mm/ms and comparison with experimental results 50
Figure 5.22 Cross-section, internal state of the material at saturation for $v = 1.57$ mm/ms 51

LIST OF ACRONYMS

ANN	Artificial Neural Network
CMM	Coordinate Measuring Machine
DRX	Diffraction Rayons-X
DSLR	Digital Single-lens Reflex
FE	Finite Element
FOD	Foreign Object Damage
LOWESS	Locally Weighted Scatterplot Smoothing
MÉF	Modèle des Éléments Finis
MMT	Machine à Mesurer Tridimensionnelle
RP	Reference Point
SAE	Society of Automotive Engineers
XRD	X-ray Diffraction

LIST OF SYMBOLS

α_R	Mass-proportional dampping coefficient
β_R	Stiffness-proportional damping coefficient
μ	Friction coefficient
ν_n	Needle's Poisson ratio
ν_t	Target's Poisson ratio
ρ_n	Needle's density
ρ_t	Target's density
σ_{axial}	Axial stress
σ_{bend}	Bending stress
σ_{ind}	Induces stress
σ^c_{max}	Maximum compressive stress
σ_{res}	Residual stress
σ_{surf}	Surface residual stress
σ_0	Target's initial yield strength
σ_x	Residual stress in x
σ^t_{max}	Maximum tensile residual stress
a_h	Arc height
A^l_p	Largest indentation area meeasured for pressure p
A^s_p	Smallest indentation area meeasured for pressure p
$Ah^{\text{Almen}}_{\text{Sat}}$	Arc height at saturation using the Almen gauge measurements
$Ah^{\text{cmm}}_{\text{Sat}}$	Arc height at saturation using the CMM measurements
$Ah^{\text{p}}_{\text{Sat}}$	Predicted arc height at saturation
$Ah(t)$	Arc height as a function of time
b	Width
$C\%$	Coverage percentage
CI	Confidence interval
D_{ind}	Indentation diameter
d^l_p	Largest indentation diameter meeasured for pressure p
d^s_p	Smallest indentation diameter meeasured for pressure p
DS	Scaling factor
E_n	Needle's Young modulus
E_t	Target's Young modulus
F	Force

$f_{i,p}$	Impact frequency of needle i for pressure p
F_x	Compressive force in X-axis
h	Thickness
H	Target's strain hardening coefficient
I	Width of the impact region of the target
I_t	Moment of inertia
l	Length
L_{bw}	Color threshold parameter
L_i^k	Coordinate of impact k in the i axis
$M_{i,j}$	Matrix of dimensions i $\times$ j
m_n	Needle's mass
M_x	Bending moment in X-axis
N	Number of impacts
$N_{\text{Sat}}^{\text{p}}$	Predicted number of impacts at saturation
p	Air pressure
r_{stylus}	CMM stylus tip radius
R_n	Needle's tip radius
R^2	Regression coefficient
$s_{i,p}$	Position of needle i at pressure p
t	Time
$T_{\text{Sat}}^{\text{Almen}}$	Saturation time using the Almen gauge measurements
$T_{\text{Sat}}^{\text{cmm}}$	Saturation time using the CMM measurements
T_p	Saturation time at pressure p
U_i	Node displacement in the i axis
$v_{i,p}$	Velocity of needle i at pressure p
V_n	Needle's volume
z	Depth
$z_{\max}$	Maximum residual stress depth
z_c	Compressive stress layer depth

CHAPITRE 1 INTRODUCTION

1.1 Introduction to needle peening

Peening consists of repeatedly striking the surface of a part with a hard object in order to induce near surface plastic deformation. Numerous types of peening processes use different means of creating the impacts, such as shot peening, flapper peening or needle peening. It is through this plastic deformation that peening induces surface compressive residual stresses that have been found to increase fatigue life. Peening is widely used in the aerospace industry to improve the fatigue life of metallic components. It is equally used as a metal forming process for thin components such as wing skins or to correct distortion due to manufacturing. Portable peening technologies, such as flapper peening, were invented in the 1960's for US army helicopter on-site damage repairs during the Vietnam war, and are increasingly used in contemporary industrial applications.

Needle peening uses relatively hard spikes, called needles, powered by a pneumatic source in order to hit the surface of a ductile workpiece. As the powered tool is pressed against and moved along the component's surface, the impacting needles stretch the impacted surface, creating indentations as seen in Figure 1.1(a). The bulk of the substrate surrounding the deformed material opposes this stretching, therefore creating a region of compressive stresses, as seen in Figure 1.1(b). The near-surface compressive layer of the deformed material hinders crack propagation under cyclic loading and therefore increases the material's fatigue life.

Needle peening results in a clean procedure that does not require media collection systems.

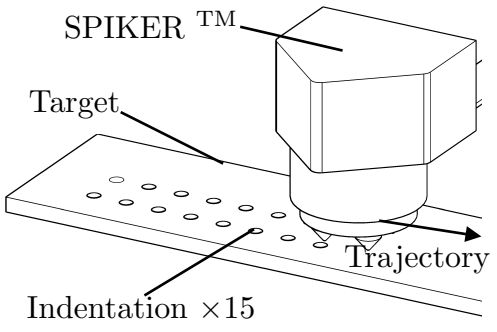

(a) Creation of indentations due to needle impacts

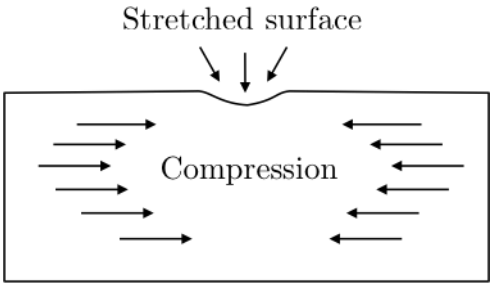

(b) Development of a compression area as a response to the indentation (Mayuram, 2013)

Figure 1.1 Generation of indentations by needle peening

This process is suitable for manufacturing environments where Foreign Object Damage (FOD) and personnel health and safety would be compromised by using a non-captive peening technology. The absence of consumable material also makes it optimal for local repairs and constitutes therefore a highly practical portable repair equipment. In overall, needle peening has a high adoption potential because of its portable design and operation features that target niche overhaul needs currently not covered by current peening equipment.

Peening parameters such as the media material properties, size, geometry, impact velocity and target material properties have an influence on the peening results. Coverage refers to the percentage of the total surface that has been impacted. Peening intensity measures the total energy transferred from the media to the material as a function of the material deformation that results from the peening induced relaxation. Standardized test strips are treated with peening equipment for different process parameters and times, and their coverage and peening intensity are measured. The measurements and inspections done to these strips are then used to determine the quality of the peening process. A thorough understanding of the relationship between process parameters and their effect on the peening results is key to ensure the correct application of this process. The Literature Review in Chapter 2 provides more details about the peening effects.

1.2 Problem definition

Shockform Aeronautique Inc. is a Quebec based pioneer in peening equipment solutions for repairs of high-value components in the aerospace and defense industries. Shockform is currently developing a portable needle peening tool called the SPIKER® for peen forming and local repairs. The SPIKER® is currently in the prototyping phase and studies show promising results. The goal is to establish needle peening as a viable alternative to manual shot peening and rotary flapper peening for niche applications.

Numerical tools have been used in the past to predict the effects of conventional shot peening. Such tools could be used to better understand the effect of the process parameters such as needle size, shape and the applied pressure on the induced forming effects in the case of needle peening. These models would provide Shockform with sufficient knowledge to optimize its design to better meet the requirements of their costumers.

1.3 Thesis overview

The objective of this study was to develop and validate numerical models for predicting the effects of needle peening, such as residual stresses and deflection of thin strips, performed with equipment currently in development. The effects of the driving process parameter (pressure) on the peening parameters (impact speed and frequency) were studied. A dynamic finite element model was developed, based on existing modelling strategies implemented for shot peening, for predicting the development of residual stresses on peened strandardized strips. A forming finite element model was used to predict the deformation of the specimens based on the residual stresses calculated by the dynamic model. The models' predictions were validated by an experimental campaign that makes use of the prototype developed by Shockform.

CHAPITRE 2 LITERATURE REVIEW

2.1 Introduction to peening

Surface treatment is used particularly in the aerospace industry to improve the fatigue life of metallic components. During peening, a workpiece is cold worked repeatedly using a hard body to plastically stretch the surface to improve its fatigue properties (Shen and Alturi, 2006). Ancient civilizations have long known that work hardening leads to harder and more durable materials. Military equipment like shields, breast plates, spear heads and swords were harder and stronger because of blacksmith hammering (Hawkinson, 1962). The evolution of peening techniques has led to the development of specialized and larger-scale technologies such as shot peening, ultrasonic peening, rotary peening and needle peening.

A component impacted with a small projectile undergoes local tensile plastic deformation. A compressive residual stress field is developed in the near-surface layer as a consequence to the continuity conditions between the elastic and the plastic deformation zones. This means that the bulk of the material opposes the plastic deformation of the indentation by a manifestation of compressive stresses in the near surface. The compressive stress field hinders crack nucleation and growth of very short surface cracks thus extending the fatigue life of peened components. A typical residual stress field produced after peening is shown in Figure 2.1 where negative residual stresses represent compressive stresses whereas positive residual stresses represent tensile stresses. This stress distribution is characterized by the value of compressive stresses at the surface σ_{surf}, the maximum compressive stresses near the surface σ^c_{max} and the depth at which the maximum is located z_{max}, the depth of the compressive residual stresses z_c, and the maximum tensile stresses found at the core of the material σ^t_{max} (Gurova et al., 2012).

2.2 Types of portable peening technologies

2.2.1 Shot peening

The most notable difference between the various types of peening is the media employed to deliver the impacts and the mechanisms by which the media is controlled. Shot peening utilizes airborne media, called shots, made from hard materials such as ceramic or hardened stainless steel. Shot peening is popular for aerospace applications ranging from manual to

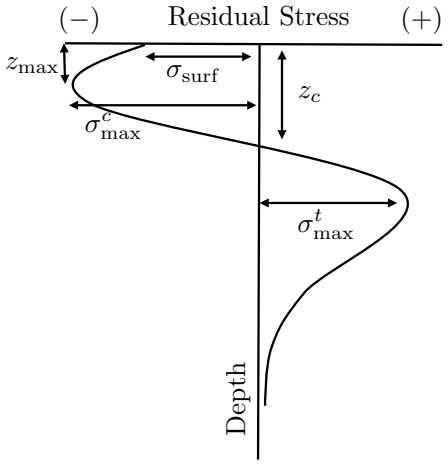

Figure 2.1 Typical induced stress profile after peening (Al-Obaid, 1990)

fully automated operations. Shot peening using nozzles is depicted in Figure 2.2(a) where shots are being targeted onto a work piece by means of pressurized air. The size of the shots can vary between 0.18 mm and 2.00 mm in diameter, and can travel at velocities between 40 and 70 m/s (Meguid et al., 1999). Media can also be projected onto a target by radially accelerating media using centrifugal high speed paddled wheels (Tekeli, 2002).

2.2.2 Rotary flap peening

Rotary flap peening was first developed by 3M for helicopters in the 1960's and it was mainly used to repair small areas by blending scratches or to repair surface damage. The setup consists of small tungsten carbide beads attached to flexible flaps that rotate around a shaft in order to impart impacts to the surface. An illustration of a typical rotary flap peening tool is shown in Figure 2.2(b). A concern revolving about flapper peening is the lack of control of the rotational speed when connected to a non-regulated source of compressed air, which

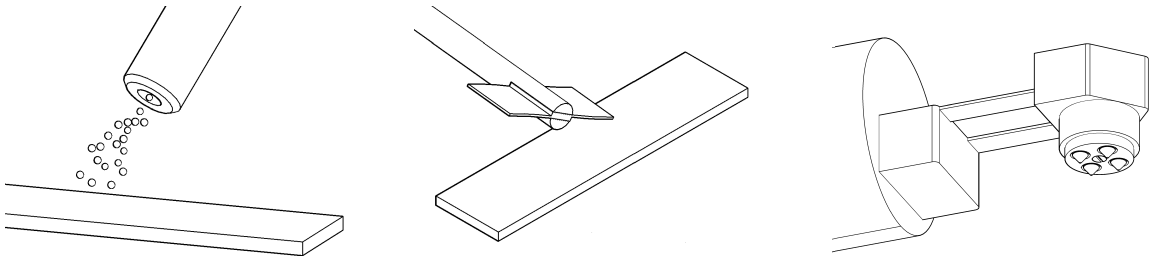

(a) Shot peening (b) Flapper peening (c) Needle peening

Figure 2.2 Types of portable peening equipment

could result in variation in peening results. Progress has been made in this field to develop more accurate controllers that would allow for a more repeatable process (Forgues et al., 2011).

2.2.3 Needle peening

Needle peening consists of a captive media method in which a gun is equipped with needles in a given arrangement. A four-needle arrangement is shown in Figure 2.2(c). When the gun is triggered, the needles are thrown against the surface, powered either pneumatically or by the vibratory effect of a sonotrode. Typical needle peening tools operate at a relatively low frequency ranging from 50 to 100 Hz, while ultrasonic impact treatment tools work up to 27 kHz (Haagensen, 1998). Needle peening is generally applied to welded areas in order to add beneficial compressive stresses to ensure the weld's life extension. Needle peening is currently used on sub-critical components given the limited experience and research on this process.

2.3 Mechanics of peening

Wohlfahrt (1984) described two different processes of localized plastic deformation that lead to a distribution of compressive stresses at the surface of the material and throughout its thickness (Figure 2.3). The first process stems from the change in the surface topography and work hardening that result from numerous and repeated impacts on the surface. The elastic-plastic stretching of the surface layer results in a maximum compressive residual stress at the surface, as seen in Figure 2.3(a), in the absence of other deformation mechanisms. The magnitude of surface residual stresses is related to the degree of plastic deformation of the surface layers. Figure 2.3(b) shows the stress field stemming from the Hertzian pressure imparted by a statically applied force F. The resulting compressive stress has a maximum value below the surface. The degree of plastic deformation underneath the point of pressure determines the maximum magnitude of the residual stress. The stress profile after shot peening combines features of the two processes.

2.4 Process monitoring

2.4.1 Almen intensity

Peening intensity is the quantity used to determine the effects of shot peening. When a relatively thin piece of metal is peened from one side, it curves in the direction of the incoming

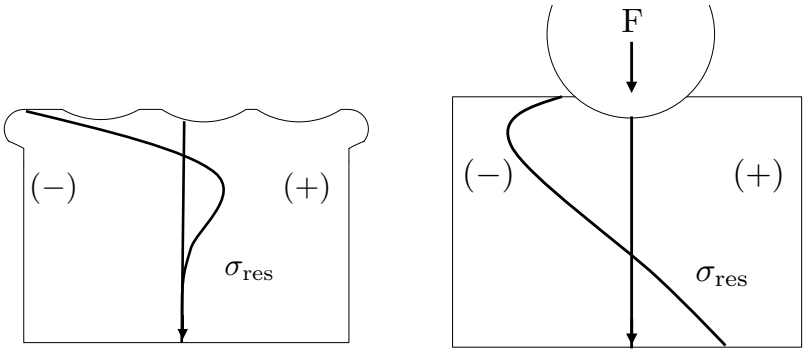

(a) Stretching the material surface as a result of multiple impacts

(b) Static pressure indentation as a result of the vertical force F

Figure 2.3 Development of residual stresses as a consequence of (a) surface layer stretching and (b) Hertzian pressure. (Wohlfahrt, 1984)

shot flow as a response to the plastic deformation induced by the impacts. Almen intensity is the measurement of the arc height deflection of a test sample; the greater the curvature, the larger is the energy transferred to the work piece. Almen and Black (1963) developed a standard process to measure the energy transfer from a shot stream into standardized samples called Almen strips. The Almen strips are made of 1070 steel and have a length $l = 76$ mm and a width $b = 19$ mm. Almen strips come in three thicknesses h: for type N, $h = 0.79$ mm; for type "A", $h = 1.29$ mm; and for type "C", $h = 2.39$ mm (SAE, 2013b).

The stages of the process by which the intensity is determined are shown in Figure 2.4. An Almen strip is bolted onto an Almen holder in order to hold the test specimen in position throughout the operation (Figure 2.4(a)). The curvature of the test strip is measured using a three-point contact gauge once the constraints are removed to determine the arc height a_h (Figure 2.4(b)). A saturation curve (Figure 2.4(c)) is obtained by peening Almen strips for different treatment times and plotting the measured arc height against peening time. The curve is characterized by the saturation point (a_h^{sat}, T), where a_h^{sat} is the arc height of an Almen strip measured at the earliest instance when doubling the exposure time increases the arc height by a maximum of 10% (SAE, 2010). The peening intensity is the value of a_h^{sat} commonly measured in thousands of an inch. Depending on the type of Almen strip used, the notation for intensity uses type as a unit signifying thousands of an inch (e.g. if the arc height at saturation on a type A strip is of .008 in., the intensity would be noted as $8A$). SAE J442 (SAE, 2013b) and SAE J443 establish the requirements of the equipment and provide guidelines for determining the peening intensity.

2.4.2 Surface coverage

Coverage is a quantity used to monitor the progression of peening on a part. The effectiveness of shot peening is believed to depend directly on coverage; incomplete or excessive coverage may be detrimental to fatigue life. Coverage is referred to as the ratio, expressed as a percentage, between the surface covered by indentations and the total surface area of the target such as:

$$C\% = \frac{\text{Area}_{\text{indented}}}{\text{Area}_{\text{total}}} \tag{2.1}$$

In a production environment, coverage is determined through visual inspection using $10X$ magnification. It is said that a surface has reached full coverage once $C\% = 98\%$ due to the examination method's limitations. Coverage beyond full coverage is determined by multiples of the time required to achieve full coverage; for example, 200% coverage is achieved by peening for twice the full coverage time. The standard practices for measuring peening coverage are detailed in SAE J2277 (SAE, 2013a).

2.5 Experimental studies on peening

2.5.1 Shot flow characterization

A study to determine the shot distribution in shot peening was performed by Gariépy et al. (2011) in order to characterize the shot stream and define input model parameters for FE simulations. A peening enclosure was modified to accommodate a Digital Single-lens Reflex (DSLR) camera with a macro lens and a flash to simulate high-speed photography. The photography parameters used were 1/200 s at $f5.6$, ISO 200 and flash at 1/28 power with a duration of 1/38500 s. Velocity of the shots was not studied as it could be controlled as a process parameter.

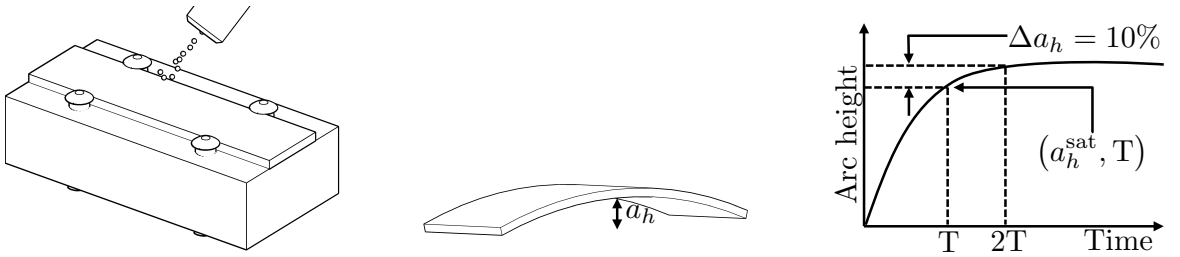

(a) Peening of an Almen strip on an Almen holder

(b) Arc height of an Almen strip after peening

(c) Saturation curve

Figure 2.4 Process to determine the intensity of peening (Miao et al., 2009)

Hribernik and Bombek (2006) developed a method to calculate the shot velocity by means of measuring the phase shift between the signals produced when shots impact a membrane over a microphone. A different approach relies on measuring the phase shift of laser waves projected perpendicularly to the shot stream allowing to calculate the average shot velocity provided the shot flow characteristics are known (Konitzer and Polanetzki, 2011). This methodology has been adopted as a continuous process control method by engine manufacturers (Badreddine, 2014).

2.5.2 Residual stress

Residual stresses are defined as the remaining stresses after manufacture and handling once the material is free of external constraints. Residual stresses develop during most manufacturing processes involving material deformation, machining or heat treatment (Sharpe, 2008).

Kobayashi et al. (1998) concluded experimentally that the residual stress field and the indentation shape due to static contact between a shot and a metallic target are different from those obtained by a dynamic impact of a sphere dropped from a height of 2 m. Tensile residual stresses are created at the center of the indentation by a dynamic impact while they are close to zero for the case of static compression. The shape of the indentations was measured with a roughness meter and the distribution of residual stresses was obtained using the X-Ray Diffraction (XRD) method. Karatas et al. (2009) applied different variations of shot peening parameters and measured the residual stresses induced in type C-1020 steel specimens using the electrochemical layer removal technique. The results were used to train an Artificial Neural Network (ANN) to determine the residual stresses as an analytical expression at different peening intensities.

Kirk (1996) measured surface residual stresses using XRD for needle peened annealed mild steel strip specimens. The effect of peening time as well as the effect of needle geometry was studied. A flat-ended, 2 mm diameter needle and a point-ended 3 mm diameter were considered. Average residual stress values were higher for the flat-ended configuration. The observed average surface stress for the needle peened samples when compared to shot peened samples was smaller. It was concluded that the indentation size was larger for the point-ended needles. Kudryavtsev et al. (2004) measured the residual stresses induced by needle peening in AISI304 stainless steel welded components using the ultrasonic method, XRD, and the neutron diffraction method. The induced compressive stresses depth correlated with the depth of plastic deformation determined by microhardness measurements. Forgues and Polanetzki (2014) compared the induced stress profiles produced by needle peening and shot

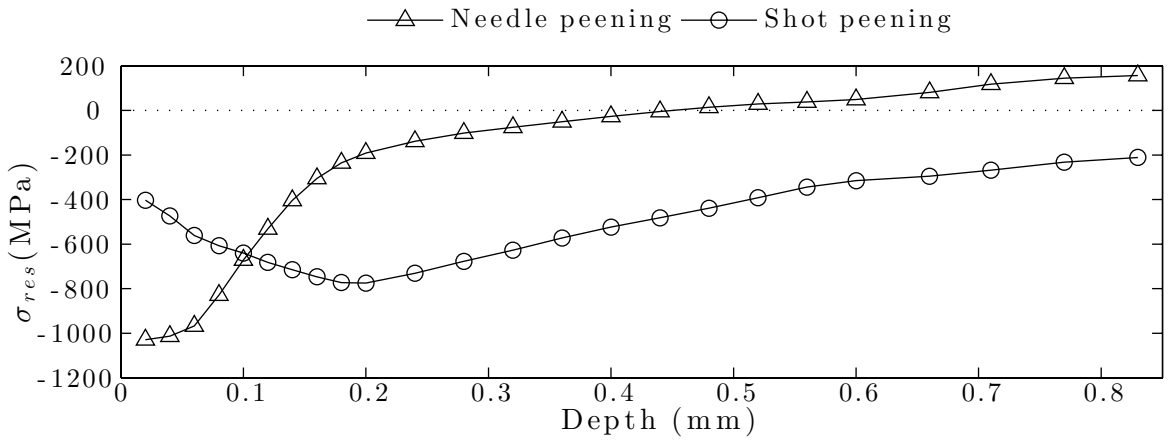

Figure 2.5 Induced stresses by needle peening and shot peening in Ti6246 (Forgues and Polanetzki, 2014)

peening on titanium alloy Ti6246 at a peening intensity of 0.10 mm A using the hole drilling method. The resulting stress profiles are shown in Figure 2.5. The figure shows that the maximum compressive stress is greater for the case of needle peening. The needle tip radius is equivalent to the shot size used, which was S330 according to SAE AMS 2430.

2.5.3 Material deformation

Wang et al. (2006) measured experimentally the arc-height of unconstrained samples in order to evaluate the response of specimens free to bend and elongate while being shot peened at pressures between 137.89 and 275.80 kPa (20 and 40 psi). The specimens were held to the surface using an adhesive film to prevent lateral displacement during peening. Cao et al. (1995) measured the deformation of constrained and free test strips after 2, 12, 48 and 80 passes of a defined shot peening stream using a surface profilometer along the longitudinal and transverse directions. It was observed in both cases that the degree of deflection increases with a greater number of passes and it stabilizes for large numbers. It was also noted that the arc height is considerably higher in the longitudinal direction than in the transverse. Gariépy et al. (2011) studied the evolution of constrained deflection and the effect of rolling direction in AA2024-T3 test samples with the same dimensions as Almen strips when attached to an Almen holder. Two sets of specimens were cut with the long axis perpendicular and parallel to the rolling direction, respectively. Small differences in arc height were observed between the sets of specimens.

Kirk (1996) measured the curvatures obtained from needle peening mild steel. Substantial curvatures were obtained for 3 mm and 6 mm thick samples. The shapes of the curves

were similar for both material thicknesses, and increasing the tool air pressure lead to faster forming rates. The relationship observed was that the curvature is inversely proportional to the square of the strip's thickness. The curvature increase with time was found to be similar to that observed in shot peening.

2.6 Analytical studies of peening results

2.6.1 Residual stresses

Li et al. (1991) studied the effect of a single impact on the residual stress state based on the fundamental approaches of Hertz which assumed linearly elastic or ideal elasto-plastic deformation. Research performed by Cao et al. (1995) delivered residual stress distribution using an analytical approach based on the shot diameters and the resulting Almen intensity. Fathallah et al. (1996) built upon this model to add the effects of friction, angle of impingement and hardness ratio between the shot and the target materials. Wang et al. (1998) obtained expressions for the compressive residual stress at the surface, the average peening dent diameter and the depth of the compressive stress field as a function of yield strength, ultimate tensile strength and peening intensity.

Unbalanced induced stresses by peening provoke stretching and bending to reach a balanced state; these manifest as arching of the Almen strips. As a consequence, an overall compressive force F_x and a bending moment M_x must be applied to the strip by the Almen holder to maintain it in a flat shape during peening (Guagliano, 2001). In Figure 2.6(a) the component remains flat after the induction of stresses σ_{ind} as a consequence of the compressive forces F_x and the bending moment M_x of the form:

$$\begin{aligned} F_x &= -\int_0^h \sigma_{\text{ind}} dz \\ M_x &= -\int_0^h \sigma_{\text{ind}} \left(\frac{h}{2} - z\right) dz \end{aligned} \tag{2.2}$$

where h is the material's thickness and z increases through the material's depth.

Figure 2.6(b) shows that axial σ_{axial} and bending σ_{bend} stresses develop as the constraints are removed; the residual stresses remain as a result. The relationship between the induced stresses and the residual stresses is given by:

$$\sigma_{\text{ind}} + \sigma_{\text{axial}} + \sigma_{\text{bend}} = \sigma_{\text{res}} \tag{2.3}$$

where σ_{ind} represents the induced stress from peening as a result of plastic deformation, σ_{axial}

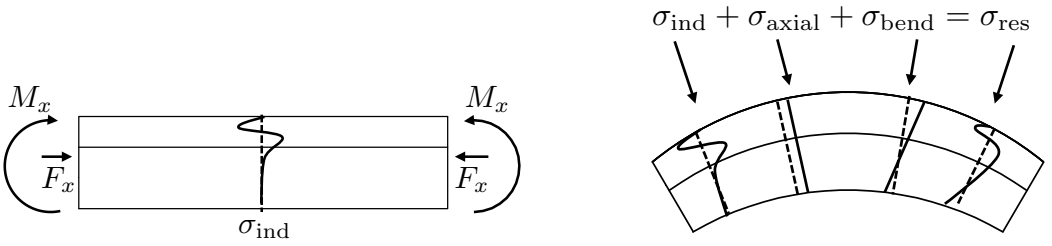

(a) Component maintained flat

(b) Component free to deform upon constraints removal

Figure 2.6 Schematic of the principle of stress forming (Miao et al., 2011)

represents the axial stress originating from material stretching, σ_{bend} the bending stresses and σ_{res} the residual stresses. This equation assumes that no reverse yielding occurs. In the case of thick materials the approximation $\sigma_{\text{ind}} \approx \sigma_{\text{res}}$ is valid since the stretching and bending deformations are negligible.

It is possible then to calculate the residual stress σ_{res} as a function of σ_{ind} through:

$$\begin{aligned}\sigma_{\text{res}} &= \sigma_{\text{ind}} + \sigma_{\text{axial}} + \sigma_{\text{bend}} \\ &= \sigma_{\text{ind}} + \frac{F_x}{h} + \frac{M_x(\frac{h}{2} - z)}{I_t} \\ &= \sigma_{\text{ind}} - \frac{1}{h}\int_0^h \sigma_{\text{ind}} dz - \frac{(\frac{h}{2} - z)}{I_t}\int_0^h \sigma_{\text{ind}} \left(\frac{h}{2} - z\right) dz\end{aligned} \tag{2.4}$$

where I_t is the moment of inertia the target component (Al-Hassani, 1999). For isotropic materials, the same equations are valid for the Y direction.

2.6.2 Material deformation and coverage

Miao et al. (2009) showed from an FE simulation that the influence of stretching on the arc height is negligible. Therefore, the arc height along the length can be approximated as:

$$AHs \approx \frac{3M_x l^2}{2Ebh^3} \tag{2.5}$$

where l is the strip's length, E is the Young's Modulus, b is the strip's width, and h its thickness. This expression shows that thinner and softer materials will experiment higher deformation under the same induced bending moment.

Guagliano et al. (1999) related the peening parameters to the maximum compressive residual stress using a non-dimensional quantity expressed as a function of the shot velocity, the

shot density as well as the target's ultimate tensile strength. The relationship allowed for calculating the needed Almen intensity and shot type required for a desired residual stress state. Furthermore, a correlation between Almen intensity and the shot velocity for a given shot type was established and validated through FE simulations and with experimental results (Guagliano, 2001).

Miao et al. (2011) related shot peening intensity and surface coverage to the number of shots impacts. With these equations, the arc height, coverage and surface roughness values at saturation were calculated independently. They concluded that for Almen and aluminum test strips, the relationship between intensities and particle velocities is almost linear. Miao et al. (2010) used the Avrami equation to predict the relationship between coverage and peening time after evaluating the topography of peened AA-2024 to determine the indentation diameters. The influence of shot velocity and peening time on residual stress and surface coverage were validated experimentally.

2.7 Numerical simulations of peening effects using the FE method

2.7.1 Dynamic impact models

The first FE models reported were for single shots hitting an axisymmetric target (Voyiadjis and Kattan, 1983). The verification of the models was achieved by comparing the contact pressure with Hertz's solution to the contact problem between two spheres; one having an infinite radius which approximated it to a half-space. For the case where plastic deformation was evidenced, verification was done by comparing the simulation results with surface topology and surface residual stresses from experiments.

The fact that current measuring techniques provide residual stress profiles averaged over a treated area makes the direct comparison of the profile along the axis of symmetry models with experimental depth measurements questionable (Schulze et al., 2008). Other limitations, such as the lack of an accurate representation of multiple and inclined impacts, have lead to the development and application of 3D dynamic FE models (Guagliano et al. (1999), Al-Hassani (1999), Meguid et al. (1999) Guagliano (2001), Zimmermann et al. (2008)). The dynamic analysis performed by Levers and Prior (1998) was used to study the induced stress profile from shot peening. Schiffner and Droste (1999) simulated the residual stress profile in an elastic-plastic surface impacted perpendicularly using different peening parameters.

Gratsy and Andrew (1996) showed that a certain amount of deflection occurs between impacts in multi-shot models for thin cross-sections. Zimmermann et al. (2008) simulated the material to tolerate deflection during peening in order to take into account the material thickness into

the development of residual stresses. They demonstrated that the model achieves more realistic predictions of in-depth compressive stresses when compared to experimental results. Miao et al. (2009), Miao et al. (2010) and Gariépy et al. (2011) successfully predicted the induced stresses in AA2024-T3 and AA2024-T351 by implementing a free-face model by constraining all displacements on the bottom surface.

Parametric studies

Majzoobi et al. (2005) researched the effects of shot peening velocity on residual stresses and the development of coverage with a periodic symmetry cell with a square contact surface for high-strength steel 4340. Hong et al. (2008) performed a parametric study to relate shot diameter, velocity and angle to the induced residual stresses using a semi-cylindrical three-dimensional single impact model. In their study Miao et al. (2009) studied the effect of impact angle with constant velocity. Miao et al. (2010) studied the effects of velocity on saturation, surface roughness, coverage and residual stresses for thin and thick AA2024 samples using a tetrahedral three dimensional model.

Effect of meshing

Since a small part of the target is subject to plastic strains, only the region close to the impact area needs to be densely refined (Hong et al., 2008). Figure 2.7(a) shows that a coarser mesh is used in the core of the material in order to reduce the number of elements in the model. Meo and Vignjevic (2003) only studied the impact area and introduced non-reflective boundary bottom elements to simulate the presence of the remaining of the part, as seen in Figure 2.7(b).

Symmetry boundary conditions were applied on the lateral ends of the models by Meguid et al. (1999) allowing the simulation of multiple impacts with a smaller model; this resulted in the mesh seen in Figure 2.8(a). Zimmermann et al. (2008) concluded that this type of symmetric boundary conditions lead to an underestimation of the in-depth residual stresses for relatively thin parts. Miao et al. (2009) divided the study area into four regions, as seen in Figure 2.9. A similar structure was used by Gariépy et al. (2011) showing consistent results while using the mesh parameters studied by Hong et al. (2008). Additionally, the effect of the symmetry boundary conditions on the area covered by indentations was studied.

Hourglassing was visually identified by Baragetti (2001) who noted zigzag shaped elements after the loading portion of the simulation was finished. Hourglass modes are found in under-integrated elements and represent non-physical, zero-energy modes of deformation. This

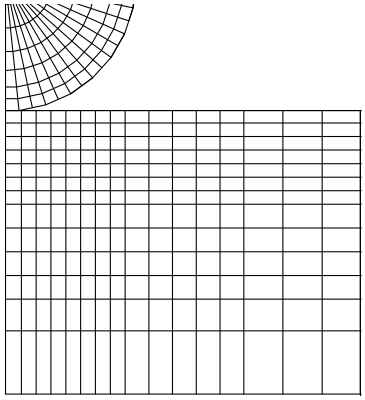

(a) 2D meshing of the contact model by Zion and Johnson (2006) showing a gradiently refined mesh that extends beyond the contact area.

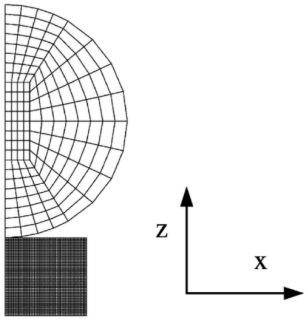

(b) 2D meshing of the contact model of Meo and Vignjevic (2003) limited to the contact area

Figure 2.7 Meshing examples for two-dimensional models

phenomenon can be solved by selecting fully integrated elements or by refining the mesh around the contact zone. Convergence studies to determine the appropriate mesh size were performed by Meguid et al. (1999), Gariépy et al. (2011) and Zimmermann et al. (2008) and the optimal mesh size is selected to be a fraction of either the shot or indentation diameter.

Effect of media distribution

Multiple impact models with predefined impact patterns were studied (Gratsy and Andrew (1996); Han et al. (2002)). Miao et al. (2009) introduced a model in which the impact location was generated randomly within given boundaries. Gariépy et al. (2011) followed a similar

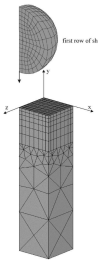

(a) Axial symmetry model by Meguid et al. (1999)

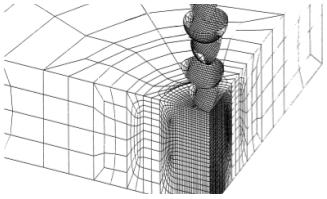

(b) Half-space, single shot model by Hong et al. (2008)

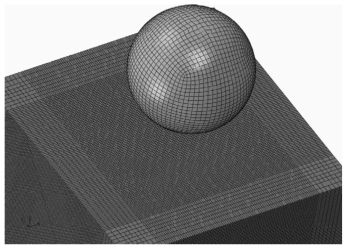

(c) Symmetry cell model by Bhuvaraghan et al. (2010)

Figure 2.8 Examples of three-dimensional FE models

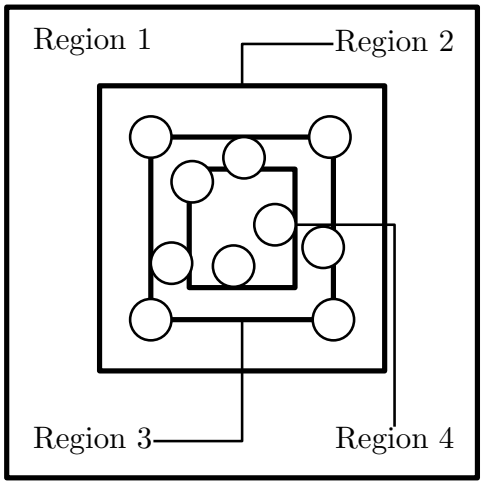

Figure 2.9 Representative surface modeling proposed by Miao et al. (2009). Region 1: aluminum surface. Region 2: fine element region. Region 3: boundary of shot centers. Region 4: representative surface.

approach and determined the impact locations by:

$$L_i^k = \frac{\texttt{randint}(-1000, 1000)}{1000} \times \frac{I}{2} \tag{2.6}$$

where L_i^k is the coordinate of impact k in the $i = \{X, Y\}$ axis, $\texttt{randint}(-1000, 1000)$ is a function that delivers a random integer between -1000 and 1000 following a normal distribution, and I is the boundaries' width. Both studies ignored the interaction between shots.

Bhuvaraghan et al. (2010) combined the FE model meshed as seen in Figure 2.8(c) with a discrete element model to account for the interaction between particles in the shot flow. Meguid et al. (1999) studied the effect of simultaneous impacts, and concluded that their effect on the resulting stress fields depends on their separation distance. Schwarzer et al. (2002) and ElTobgy and Elbestawi (2004) used three-dimensional models to study the simultaneity and close succession of impacts on the peening results. The study carried by Gariépy et al. (2011) concluded that simultaneous impacts were separated enough to ignore this effect in simulations. Zimmermann et al. (2010) determined that while the deterministic and the randomly generated impact models provided a good approximation of shot peening results in terms of residual stresses, the latter resulted in a more accurate prediction because of the more realistic assessment of surface topography.

Effect of shot deformation

Many studies including that of Han et al. (2002) assumed shots as rigid bodies to reduce calculation time. This assumption is no longer valid when dealing with harder materials for which the yield strength of the target and shot are in the same order (Schulze et al., 2008). Mori et al. (1994), Rouhaud and Deslaef (2002), Hirai et al. (2005) and Zion and Johnson (2006) studied the elastic and elasto-plastic deformation of the shot and it was concluded that a yield stress ratio of 2 between the shot and the target does not lead to plastic deformation of the shot. In the case where the media should deform, ignoring this effect may lead to an overestimation of the magnitude and depth of the maximum compressive residual stress.

Stress waves and damping

Stress waves were found to reflect at the model's boundaries, leading to stress oscillations in dynamic shot peening models with small dimensions. Al-Hassani (1999), Schwarzer et al. (2002), Klemenz et al. (2005), Bhuvaraghan et al. (2010) and Zimmermann et al. (2008) employed infinite elements to avoid the presence of stress waves reflection. Guagliano (2001) agreed that the stress in the plate will oscillate around an average value, which they took to be the stable residual stress. ElTobgy and Elbestawi (2004) and Meguid et al. (1999) applied numerical damping in the form of stiffness and mass proportional damping in `ANSYS LS-DYNA`. Gariépy et al. (2011) used Rayleigh damping with the stiffness-proportional damping coefficient $\beta_R = 0.75$ ns and mass-proportional damping $\alpha_R = 8 \times 10^{-5}$ s^{-1} in `ABAQUS`. Their selection of damping parameters did not affect notably the impact behaviour and remarked that damping is but a numerical tool and it does not represent actual physical damping properties of the material. Meo and Vignjevic (2003) introduced a non-reflective boundary surface to simulate the presence of additional substrate for thicker components.

Effect of contact friction

Friction was considered as an influencing parameter on the results of peening. Meguid et al. (1999) determined that the presence of friction, in the form of the friction coefficient μ, between shots and the surface leads to a decrease in surface plastic deformation and surface residual stresses. Similar conclusions on the effect of friction were studied by Mori et al. (1994), Han and Peric (2000), Zion and Johnson (2006) showing that friction does not have a significant effect in the variation of residual stresses and plastic strains for $0.1 \leq \mu \leq 0.5$. Miao et al. (2009), Miao et al. (2010) and Gariépy et al. (2011) adopted for $\mu = 0.2$. Bhuvaraghan et al. (2010) opted to ignore the effects of friction.

Thermal effects

Evans (2002) studied thermal effects in stainless steel, titanium and aluminum alloys. They concluded that thermal strains have no significant influence in the development of residual stresses when there is no inter-material thermal conduction and all the induced heat remains in the deformation zone. A combined mechanical/isothermal single impact simulation done by ElTobgy and Elbestawi (2004) confirmed this conclusion. Rouquette et al. (2009) noted high surface temperatures reaching up to 180 °C in the impact area. Thermal expansion leads to a significant reduction in the residual stress amplitude. There could be an overestimation of the temperatures attributed to the fact that the shot was considered rigid, and no energy was lost to its deformation.

2.7.2 Material constitutive theory

Strain-rate sensitivity

Kobayashi et al. (1998) demonstrated experimentally the difference between the static and the dynamic model solutions of a single indentation. Their study concluded that this effect could be attributed to the strain rate sensitivity of the model, which is ignored in the static loading case. Chen et al. (2014) evaluated the effect of rate-dependent behavior of 4340 steel by conducting two FE simulations. They first assumed no strain-rate sensitivity; the second case incorporated strain rates up to 10^5 s^{-1}. It was noted that the strain rate effects lead to a reduction in the plastic zone and an increase in the resulting residual stress for the same impact energy. The increase in the amplitude of the residual stress field leads to a larger arc deformation for rate sensitive materials.

Meguid showed numerically that plastic strains up to 6×10^5 s^{-1} are present during shot peening. Bhuvaraghan et al. (2010) considered strain-rate dependency into the determination of the elastic-plastic properties of IN718. The properties were obtained using the Johnson-Cook equation. This implies that subsequent impacts will hit a harder surface. Mylonas and Labeas (2011) concluded that for high strain values the deformation rate plays a significant influence on flow stresses affecting the shape of the indentations. The effect of train-rate sensitivity was neglected in more recent studyies by Miao et al. (2009) and Gariépy et al. (2011).

Material hardening laws

The degree of cold work is important in the simulation of shot peening as the work-hardened material may show modified properties when compared to the untreated material as noted by Mylonas and Labeas (2011). Isotropic hardening describes a yield surface that expands equally in all directions on a plane. It implies that an increase in tensile yield strength results in an equal increase in compressive yield. Kinematic hardening describes a constant yield surface that translates in the direction of yielding, otherwise known as the Bauschinger effect. It predicts that an increase in tensile yield strength produces a corresponding decrease in compressive yield strength. Elastic-perfectly-plastic materials exhibit no hardening.

The influence of elastic-perfectly plastic and elasto-plastic material deformation behavior with isotropic strain hardening was studied by Kral et al. (1993) for a single impact. Miao et al. (2009) assumed an isotropic bilinear hardening law for their three-dimensional random peening simulation. Mylonas and Labeas (2011) applied a multi-linear elastic-plastic material model with kinematic hardening for AA7449-T7651. Klemenz et al. (2005) proposed an elasto-viscoplastic material model with combined isotropic-kinematic hardening to describe cyclic deformation. Gariépy et al. (2011) and Rouhaud et al. (2005) showed that using a kinematic hardening model can lead to a significant decrease of compressive residual stresses compared to isotropic hardening due to the reversed plastic flow that occurs during unloading.

Gariépy et al. (2011) performed low-cycle, high-strain cyclic mechanical testing of unpeened material in order to develop a material constitutive law for shot peening. The test samples made from AA2024-T351 were tested at a rate of 8×10^{-5} s^{-1}. Monotonic and cyclic yield stresses were determined with the 0.2% method at different strain amplitudes. Majzoobi et al. (2005) obtained the Johnson-Cook constants from stress-strain curves to consider strain-rate sensitivity for steel plates.

2.7.3 Peen forming

Peen forming is a dieless metal forming technique in which the surface of a component is bombarded by high speed shots that induce a thin layer of plastic deformation near the surface (Miao et al., 2011). These deformations induce an isotropic stress profile that causes the component to curve towards the peening direction. Macro models are commonly developed to simulate peen forming and to predict the component's curvature based on peening parameters (Schulze et al., 2008). Multiple impact equivalent approaches have been introduced so as to avoid simulating the millions of shots required to peen larger components (Gariépy et al., 2011). The equivalent "squeeze pressure" was introduced to shot peening by Gratsy and

Andrew (1996) in which yielding of the surface elements was forced by the introduction of a squeezing pressure in order to obtain plastic deformation an residual stresses. Levers and Prior (1998) and Zeng (2002) made use of the thermal loading method by creating thermal strains to introduce stress distributions. In these cases, the temperature was only used as a numerical tool and does not represent the increase in temperature involved in the process.

Chen et al. (2014) suggested a two-step process approach to simulate the arc height development. The first step consists of repeated spherical impingement of an Almen strip. Symmetry boundary conditions were used to represent a quarter of a test strip mounted on an Almen holder. The second step consisted of balancing the internal stresses once the part is peened and later removed from its constraints. It was found that the arc height increases with the number of impacts and it reaches an asymptotic value; a behavior observed in the shot peening process while developing saturation curves.

In order to avoid peening a full part Gariépy et al. (2011) proposed a dynamic impact model to simulate the peening in a periodic cell. The forming model would then be used to determine the arc height based on an uniform coverage of what would be an Almen strip-sized component. The following assumptions were made:

a) Normal and uniform peening generates induced stresses at the component scale that only depend on depth, meaning these are uniform in the $X - Y$ plane.

b) The effect of trajectory is neglected when modeling multiple passes.

c) Miao et al. (2009) determined the initial rolling stresses by XRD and concluded that the development of near-surface induced stresses is almost insensitive to the initial rolling stresses.

d) Peening of the surface does not lead to severe plastic deformation at the material's core.

e) Induced surface stresses are those calculated from the dynamic impact model.

CHAPITRE 3 PROJECT RATIONALLE AND OBJECTIVES

The literature review revealed the following:

- The repeated action of impacting the surface of a ductile workpiece induces stresses as a result of the surface stretching. The resistance of the material's bulk to these plastic deformations leads to the development of compressive residual stresses in the near-surface that improve fatigue properties of the treated target and a layer of tensile stresses develops within the material's depth. Portable surface treatments techniques, such as shot peening and needle peening, are capable of providing these enhanced material properties.

- Thin samples exhibit an arc-like deflection as a result of stress-rebalancing to reach equilibrium. The deflection magnitude is commonly used to define the peening intensity as a quantity that serves as process control. Experimental campaigns have studied the effect that certain process parameters bear on the results of peening, particularly in the development of residual stresses and the associated material deflection. Knowledge of the material and contact properties of the peening system are therefore required in order to properly develop a robust process. These are obtained either by characterization of the equipment or the material.

- The characterization of AA2024-T3/T51 performed by Gariépy et al. (2011) provides good reference to investigate the effects of different types of peening on the same material. Similar assumptions to those listed in Chapter 2 can be made regarding the model types and geometry, material sensitivity to strain-rate and hardening. The fact that it is relatively insensitive to high strain rates and that its reaction to shot peening has been extensively studied at the Laboratory of Multiscale Mechanics (LM2) of l'École Polytechnique de Montréal make it an ideal candidate for this study since material characterization is not in the scope of this project.

- Very little is known about the effects of needle peening for the development of induced stresses. No numerical simulation exists in the public literature for simulating the residual stresses and material deflection due to needle peening. An experimental and numerical study is needed in order to better understand the process and pave its introduction for potential business applications. The random dynamic FE model developed by Miao et al. (2009) can accurately predict the development of induced stresses by peening AA2024. Similar assumptions regarding contact friction and shot rigidity may

apply to the case of needle peening. The model dimensions studied by Gariépy et al. (2011) may be used in order to adapt the models to the geometrical and operational parameters of needle peening.

The questions raised during the literature review are:

1. Can the existing assumptions and conclusions derived from the research of shot peening be tailored to model needle peening based on the equipment's process parameters?
2. Assuming the target material properties from previous studies and a random distribution of impacts, can the newly developed models accurately predict the effects of needle peening (induced stresses and material deflection) on AA2024-T3 Almen strip-shaped samples?

The answering of these questions have lead to the following objectives:

1. Characterize the operation of needle peening equipment and experimentally study the effects of its application on AA2024-T3.
2. Develop and validate numerical models for predicting the induced stresses and the material deflection as a result of the application of needle peening.

The research project guided under these objectives is presented through the research methodology (Chapter 4) of the equipment characterization and the simulation strategy of needle peening using the FE method. The results obtained (Chapter 5) from the numerical simulations are presented and validated using experimental results. A general discussion of the results (Chapter 6) and a conclusion (Chapter 7) follow.

CHAPITRE 4 RESEARCH METHODOLOGY

4.1 Needle peening application on AA2024 and process characterization

This section describes in procedural form the tasks performed in order to analyze the behavior of the portable needle peening equipment SPIKER^{TM}. The equipment geometry was characterized based on the engineering drawings given by the industrial partner. High speed camera recording was used to study the dynamics of the equipment during its application. A digital image processing model was developed to quantify the tool's operational parameters. The reaction of AA2024 was studied through an experimental campaign. Test specimens were peened using the needle peening equipment. The specimens' deflection was measured after different treatment configurations. Surface plastic deformations were quantified in terms of the indentation diameters. Finally, the residual stress profile was determined for one of the samples.

4.1.1 Equipment characterization

The equipment used for the study is a portable pneumatic needle peening equipment in prototype form. Figure 4.1(a) shows the equipment as well as its key components. The air powered handheld device features four protruding needles traveling along their axes due to the pneumatic pressure and internal mechanisms. The needles' geometry is shown in Figure 4.1(b); only the needle tip diameter is shown as the other dimensions are confidential. These needles are attached to the pneumatic sleeves connected to pistons. The head is covered by a teflon ring that controls the stand-off distance during peening. The head is attached

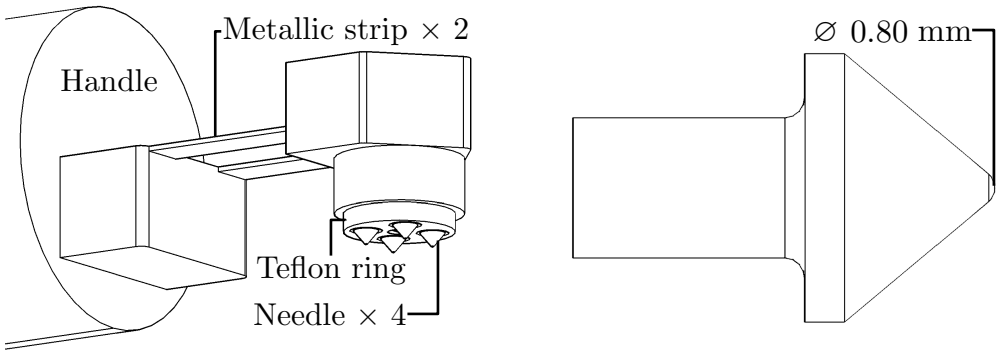

(a) SPIKER^{TM} head components (b) Side-view of an individual needle

Figure 4.1 Simplified representation of the needle peening equipment prototype

by a pair of thin metallic sheets that bend in order to ensure that the contact between the equipment and the work piece is continuous.

A 3D model was drafted using `AUTOCAD`^{TM}2015 for Mac, version J.31.M.313 using the geometrical information provided in the engineering drawings. The volume of the needle V_n was calculated using the `VOLUME` function. The needles' density ρ_n was obtained from the manufacturer and their masses m_n were computed as

$$m_n = \rho_n V_n \tag{4.1}$$

High-speed camera recording

High speed photography was used to analyze the dynamics of the needles during peening under various operation conditions. The tool was held into place by means of two 1 EMT 1308 galvanized steel straps, as seen in Figure 4.2(a). A high-speed recording camera MotionBlitz ® Cube4 was used with a 60 mm $f2.8$ lens perpendicular to the $X - Z$ plane. The tool head was rotated slightly so as to have the four needles in frame simultaneously. Two 1200 W light sources were positioned behind the camera pointing at the tool to improve lighting conditions for obtaining images of optimal quality. A clear white photography screen was positioned in the background for an improved contrast.

The operation parameters were selected using the tooling's internal digital controller for air pressure $p = 68.95$, 103.42, 137.89, 172.37, and 206.84 kPa (10, 15, 20, 25, and 30 psi). The air pressure range exceeds the lower and upper typical operational limits recommended by equipment manufacturer. The frames were recorded individually as `.bmp` files at a recording frequency of 5000 fps at a resolution of 480 × 206 pp. For each of the operating pressures, the recording lasted 200 ms, meaning that 1000 frames were obtained per pressure. The time

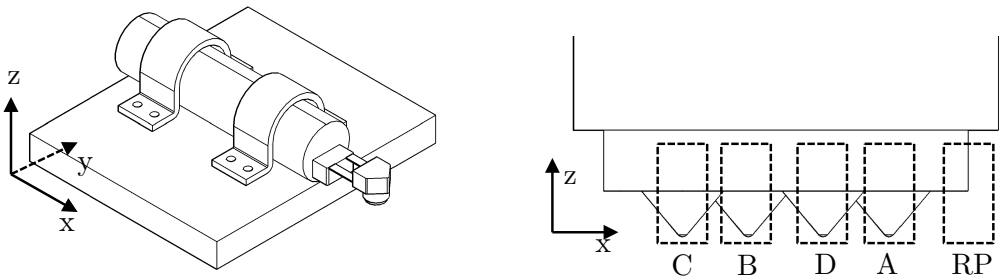

(a) Equipment holding fixture for camera recording.

(b) Frame subdivision.

Figure 4.2 High-speed camera recording set-up

step between frames was 200 μs. In total, 5000 images were obtained. The teflon ring was removed from the assembly in order to better appreciate the complete needle movement.

Digital image processing

A program was coded using `MATLAB` to analyze the collection of images obtained from the high-speed camera recording. A subroutine divided each frame into sub-frames to analyze each needle individually, as well as the edge of the tool head which served as a Reference Point (RP). Figure 4.2(b) shows the division of the frame into sub-frames highlighting the features of interest. Each sub-frame was wide enough to only include one feature without interfering with adjacent elements and high enough to capture the complete trajectory. The needles were labeled as needle A, needle B, needle C and needle D and the edge of the tool as RP.

The advantage of handling the images as `.bmp` files is that these can be read as matrices with dimensions matching their resolutions. This means that each pixel is represented as an element in the matrix with a value $M_{i,j} \in [0, 255]$, where i is the row and j is the column of that element. The images were converted to binary image by thresholding. A sensitivity analysis was performed and a color threshold parameter of $L_{BW} = 0.3078$ was selected in order to better define the contour of each feature. By applying this value, the sub-frames were converted into binary matrices with allowed values of $M_{i,j} = 255$ for white and $M_{i,j} = 0$ for black; the black represented the feature and the white the background.

The lowermost black pixel in each frame was determined using a `MATLAB` subroutine. A family of subframes was defined as the collection of frames obtained from the high-speed camera recording for a specific feature of interest. For a given family of sub-frames, beginning with the leftmost column of the first sub-frame, the lowest location of a pixel with an equivalent matrix value of $M_{i,j} = 0$ was identified and stored temporarily as a local and global minimum. The program continued with the next column and compared its local minimum with the global minimum. If column's j minimum was greater than the global minimum a new global minimum was defined. The program continued scanning horizontally and the global minimum for that subframe was obtained. A global minimum was identified for each frame (measured as vertical pixel position) in the family of sub-frames. This procedure was repeated for the five features (Needle A, Needle B, Needle C and Needle D and RP) and for $p = 68.95$, 103.42, 137.89, 172.37, and 206.84 kPa (10, 15, 20, 25, and 30 psi)

The position of the RP was subtracted from that of the needle tip. Figure 4.3 shows a comparison between typically measured points, a moving 5-span average regression, and

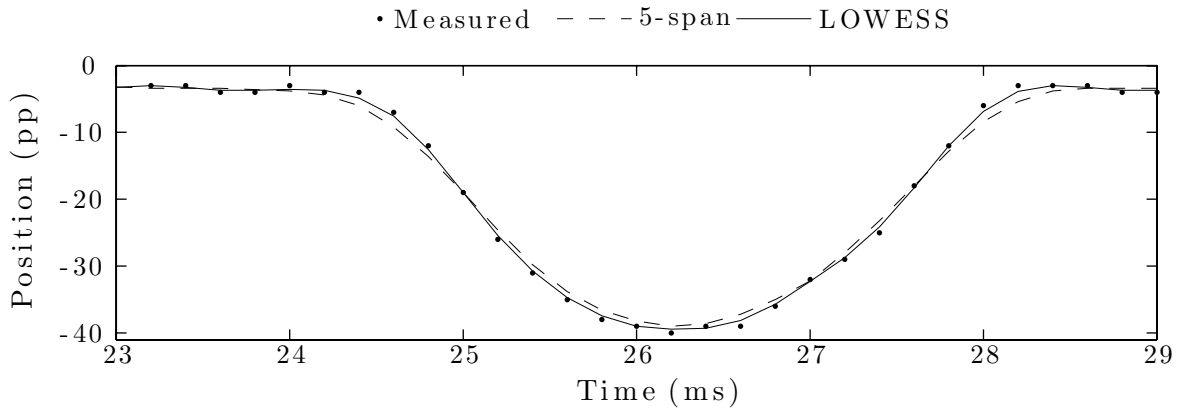

Figure 4.3 Comparison of regression fit smoothening functions

Locally Weighted Scatterplot Smoothing (LOWESS). A smoothening function of the type 5-span moving average was applied in order to reduce pixel noise for uneven lighting conditions. A conversion factor of 1 pp = 0.055 mm was used to relate vertical pixel position to vertical displacement in millimeters. This was obtained by averaging the product of the number of pixels of key geometrical features by their dimensions obtained from the engineering drawing. The needle i velocity $v_{i,p}(t)$ was obtained by calculating the derivative of position relative to time. The stand-off distance between the protruding surface of the needles and the impact surface was controlled by the teflon ring. The teflon ring represents a stand-off distance of 0.64 mm. Figure 4.4 shows a typical plot for a needle's position for $t \in [0, 100]$ and the separation between the tool and the impact surface by means of the teflon ring. The average impact velocity $\bar{v}_{i,p}$ of a needle i at a pressure p was calculated by averaging the velocities

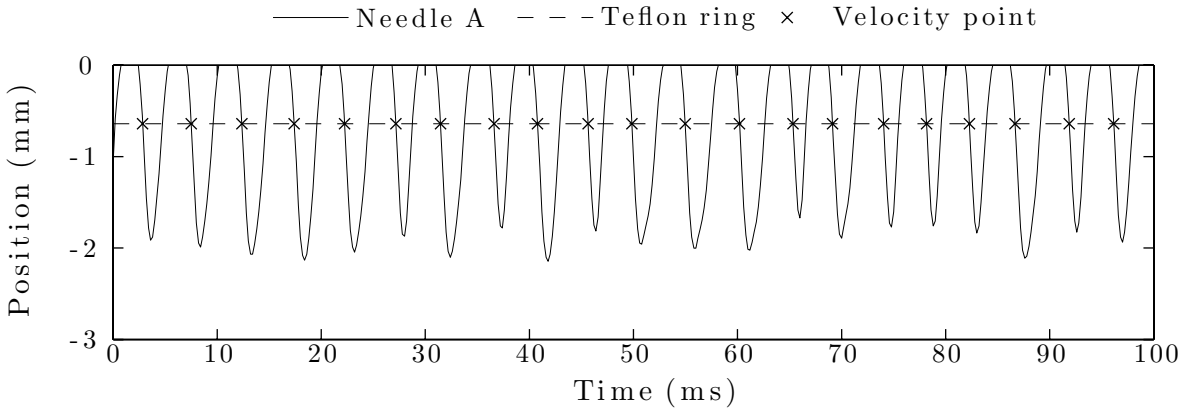

Figure 4.4 Typical needle tip position as a function of time and computation of velocity at impact location

at the intersections between $s_{i,p}(t)$ and $y = 0.64$ when $v_{i,p}(t) < 0$ for $t \in [0, 200]$. These are marked in Figure 4.4 and represent the instances when a needle would impact the material surface. The same procedure was followed for each needle for a given pressure p. The average needle velocity v_p at a pressure p was calculated by averaging $\bar{v}_{i,p}$ for i =needles A, B, C, and D. Average needle impact velocities were calculated for p = 68.95, 103.42, 137.89, 172.37, and 206.84 kPa (10, 15, 20, 25, and 30 psi).

4.1.2 Experimental procedures

Saturation tests

Saturation tests are performed to study the material response in terms of intensity at a given set of peening parameters. As only one needle geometry was selected for this study, the sole varying parameter was the air pressure for p = 68.95, 103.42, 137.89, 172.37, and 206.84 kPa (10, 15, 20, 25, and 30 psi). AA2024-T3 1.6 mm thick sheets were cut into test specimens with dimensions similar to those of a standardized Almen strip according to SAE J442 (SAE, 2013b). Six (6) samples were obtained for each pressure p for a total of 30 samples. Sample preparation consisted in cleaning the surfaces of from dust and grease using isopropyl alcohol. The incremental treatment times chosen to develop a saturation curve were t =30, 60, 120, 240 and 480 s. Before peening, the initial deflection ah_0 was measured using an Almen gauge according to SAE J442 and documented. One (1) test specimen was mounted on an Almen holder in preparation for treatment, as shown in Figure 4.5. The bolts were torqued enough to restrain sample movement without the use of excessive force. The sample would be continuously peened for a single treatment time t for each operating pressure. Since there are no specifications currently available for handheld needle peening, peening was performed in small circular motions. Attention was given to ensure uniform coverage throughout the work surface.

Once the treatment time t was achieved, the sample was removed from the Almen holder and its ah_t was measured using an Almen gauge and documented. The arc height for the treatment time ah_t was plotted. The saturation curve was produced by plotting the arc heights for the different treatment times and by obtaining a best fit. The saturation point $(a_{h,p}^{sat}, T_p)$ for a pressure p was determined as the first instance in the curve when doubling the treatment time t yielded an increase of 10% in arc height. An additional sample was peened for T_p. The procedure was repeated for all operating pressures. A sample could not be repeened once it was removed from the Almen holder.

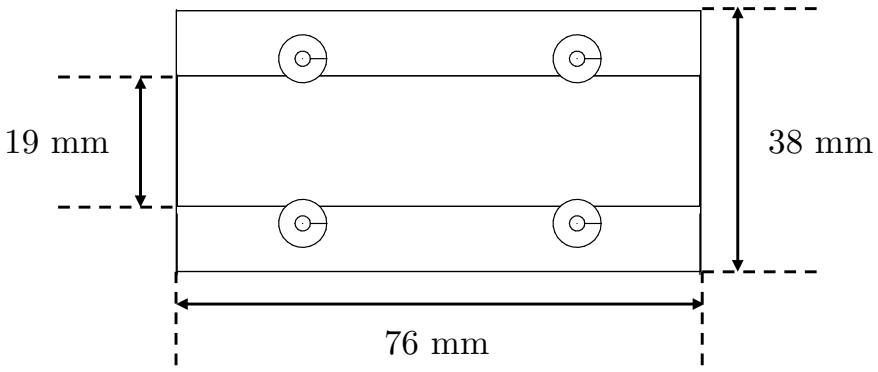

Figure 4.5 Test sample attached to an Almen holder and dimensions

Specimen deflection

Sample deflection was measured using a Coordinate Measuring Machine (CMM) in addition to the arc height measurement using an Almen gauge as part of the saturation tests. The CMM measurements were obtained at the Metrology Laboratory of École Polytechnique de Montréal. The measuring probe was a MITUTOYO one side cut stylus model SPH-71. The stylus had a tip radius $r_{\text{stylus}} = 25$ μm and a chamfer of 12 °. The stylus was attached to a MITUTOYO straight arm model ABH-71 and displacement was controlled by the CMM. Measurements were obtained in the samples' longitudinal and the transverse directions for 69.96 mm and 16.95 mm for the specimen's length and width, respectively, along its centre line. The position of the needle tip was registered at at intervals of 0.05 mm. Perpendicularity between the stylus displacement and long and short sample axes was ensured. Surface roughness measurements were not obtained for this study.

Indentation analysis

Samples submitted to low treatment times were used to assess the indentations geometry. One (1) sample per operation pressure was analyzed using a Leitz Metallovert microscope. Software `Clemex Captiva` version 6.0 was used for image analysis and light control. The images were obtained at the Metallurgy Laboratory of École Polytechnique de Montréal. A magnification of $\times 100$ was used to obtain a general appreciation of the indentation distribution over a small area in the sample. Magnification of $\times 200$ was used to obtain a more detailed view of single indentations for accurate measurement. A thin metallic strap was used to flatten the samples as to avoid image distortion and sample movement. In-plane images parallel to the peened surface were obtained to measure indentation diameter d_{ind}. Penetration depth was not obtained for this study.

Residual stress determination

The residual stress profile was obtained by determining the residual stresses at different material depths. The XRD was employed to measure the residual stress profile corresponding to pressure $p = 137.89$ kPa (20 psi) at saturation. For each measurement, the surface material was electropolished in an area of 2 mm in diameter. The X-ray aperture was 2×5 mm. The measurements were obtained at $z = 0$, 0.062 , 0.099, 0.149, 0.195, 0.419, 0.495, and 0.596 mm and compensated using gradient and depth correction. The measurement points locations were determined based on typical stress distributions found in literature. The test was done at PROTO Manufacturing in Oldcastle, Ontario.

4.2 Numerical analysis

Numerical tools were developed to determine the induced residual stresses in an AA2024-T3 sample after needle peening and study the peening parameters' effects. A random multiple impact model was built to simulate numerous needles impacting against a workpiece. The induced stress distribution was obtained from the model. A peen forming model calculated the material deflection based in the induced stresses.

4.2.1 FE impact model

The FE analysis software `ANSYS` was used in combination with a `MATLAB` program to generate nodes for the impacts coordinates. The program allowed for generating a parametric FE model featuring the mesh, number of impacts, material properties, boundary conditions, and contact parameters. The target material parameters were a Young's Modulus $E_t = 71.7$ GPa, a Poisson's ratio $\nu_t = 0.33$, and a density $\rho_t = 2810$ kg/m^3. The material was assumed to follow a bilinear isotropic hardening law, with an initial yield strength $\sigma_0 = 379$ MPa and a strain-hardening coefficient $H = 810$ MPa. Reduced integration solid elements `SOLID164` were chosen to model the target material as they support nonlinear features required for explicit dynamic analysis. All these properties were obtained from Gariépy et al. (2011).

The needle material properties obeyed those of carbon tungsten. The needles were represented as half-spheres to reduce the model size. The material properties used in the model were $E_n = 643$ GPa, $\rho_n = 15630$ kg/m^3, and Poisson's ratio $\nu_n = 0.21$ (Cardarelli, 2008). The needle tip radius $R_n = 0.4$ mm was selected based on the prototype's drawings. Based on the ratio $E_t/E_n = 8.96$, it was assumed that the needles did not experience significant plastic deformation and were therefore considered as rigid bodies (plastic deformation is expected for $E_n/E_t < 2$). The needles were approximated as rigid hemispheres meshed with `SHELL163`

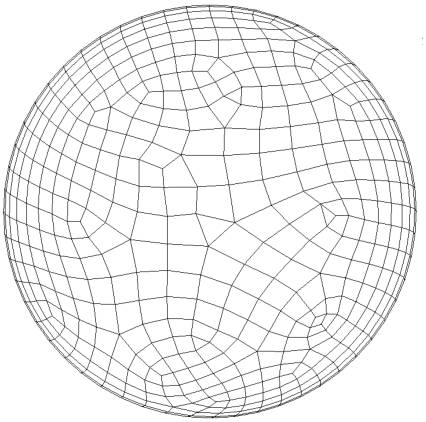

(a) Needle tip FE tessellation

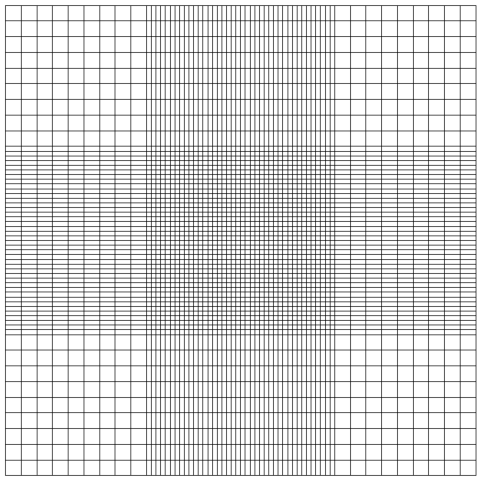

(b) Target FE tessellation

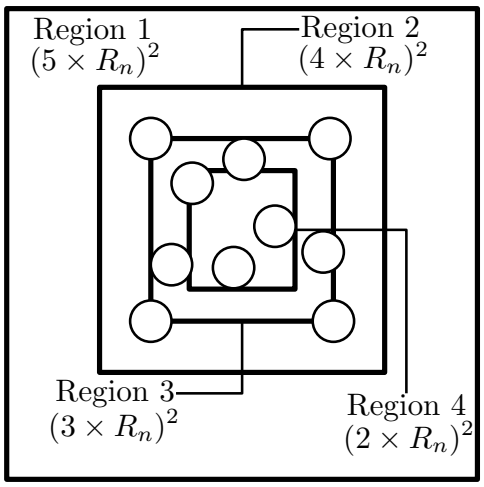

(c) Meshing regions

Figure 4.6 Three-dimensional FE model

elements, as seen in Figure 4.6(a), as it is compatible with explicit dynamic analysis. The needles tip were given the mass properties corresponding to the full needle as calculated in Section 4.1.1, and adding the mass of the piston that moves the needles.

The FE model consisted of an array of four square regions stacked in two layers with different

Table 4.1 FE mesh geometry

Mesh type	Dimension	Location X-Y	Location Z
Fine	$0.1 \times R_n$	Region 2, 3, 4	Upper layer
Coarse	$0.3 \times R_n$	Region 1	Lower layer
Needle	$1.2 \times R_n$	-	-

mesh sizes, as shown in Figure 4.6(b). In figure 4.6(c), region 1 represents the target material model dimensions, region 2 represents the area of high expected plastic deformation, region 3 the impact area, and region 4 the area where induced stresses were calculated. The model depth in the Z-axis was 1.6 mm to match the sample thickness. A fine mesh was implemented based on the investigation by Gariépy et al. (2011). A coarse mesh was selected for the lower layers and the outer regions of the model to reduce the number of elements. Table 4.1 shows the different mesh sizes and the regions of their implementation. The damping parameters $\alpha_R = 0.75$ ns and $\beta_R = 8 \times 10^{-5}$ s were used to introduce Rayleigh damping in order to reduce stress oscillations (Gariépy et al., 2011). A convergence study was done to validate the dimensions selected for the fine and coarse meshing.

It was determined that the needles impacted randomly on the surface as there is no control over the peening trajectory when it comes to manual peening. The program would generate N impacts, and their coordinates were generated randomly according to:

$$L_k^i = I \times (2 \times \texttt{rand}(0,1) - 1) \tag{4.2}$$

where $i = \{X, Y\}$, L_X^k and L_Y^k are the X and Y coordinates at the center of the needle k, `rand`(0,1) is a number in the range of [0,1] from a uniform random distribution and I is the width of region 3. `LS-DYNA` was used to simulate the dynamic impacts between the needles and the target.

The needle velocity was input as an initial boundary condition. The velocity was selected from the results of the equipment characterization defined in Section 3.1. All impacts were considered normal because during operation, the constant contact of the teflon ring against the surface ensures perpendicularity. Contact friction parameter $\mu = 0.2$ was initially selected based on the assumption that $0.1 < \mu < 0.5$ shows no significant effect in the distribution of the induced residual stresses. All displacements were constrained at the bottom of the target. The dynamic simulation was considered to be completed once there was no contact between the last needle ($k = N$) and the target after the impact. The simulations were done at l'École Polytechnique de Montréal, on an Intel®Xeon®CPU running at 2.27 GHz and a memory of 24 GB RAM with 24 processors.

For normal impacts, the average stress profiles are almost identical in the X-Y plane (Zimmermann et al., 2010); only through-depth average stress profiles $\bar{\sigma}_x(z)$ were obtained. The average residual stress $\bar{\sigma}_x(z = 0)$ was obtained by averaging the *X-stress* nodal solutions of the nodes in region 4 at the surface of the target. The average residual stress profile $\bar{\sigma}_x(z)$ was obtained by obtaining the in-plane average residual stress at different depths for $z \in [0, 1.6]$. Additionally, through-depth average plastic strains were obtained at the specimen's center

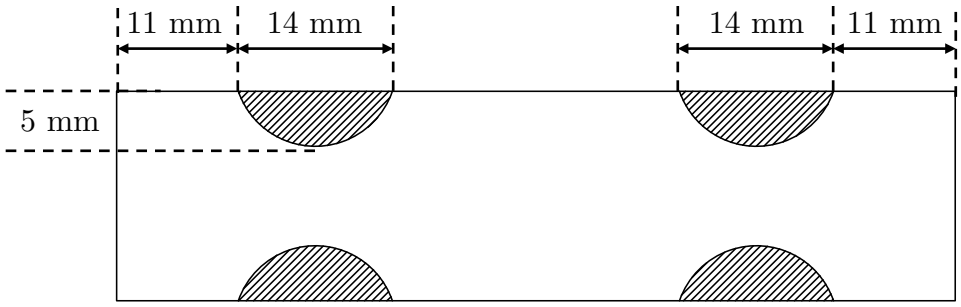

Figure 4.7 Unpeened areas in test specimen after needle peening

line.

4.2.2 Specimen deflection

The induced stresses obtained from the dynamic impact model represent the material in an unbalanced state. The FE model developed by Gariépy et al. (2011) was used to predict the specimen deflection at the center by defining the residual stresses as initial boundary conditions. This method was selected to avoid simulating peening over a complete specimen as it would be computationally ineffective. The residual stress profile was assumed uniform along the X-Y plane and only varied in depth. The material properties for the specimen were the same as established before. The physical specimens used in the experimental campaign showed no indentations in the shaded areas shown in Figure 4.7. The material in the proximity of the bolts that held the strips to the Almen holder was left untreated. It was assumed that the development of induced stresses was not affected by the initial forming stresses to roll the material into sheets. Moreover, initial rolling stresses were not considered in this study. Saturation curves were created in order to calculate the saturation point.

CHAPITRE 5 RESULTS

5.1 Needle peening application on AA2024 and process characterization

5.1.1 Equipment characterization

The average impact velocity $v_{i,p}$ for a needle $i = \{A, B, C, D\}$ per pressure p obtained from the high-speed characterization is presented Figure 5.1. It is observed that the relationship between the velocity at impact and the air pressure is almost linear. This trend was expected since increasing the air pressure provides more energy to activate the needles. The impact velocity of needle A is the most sensitive to an increase of air pressure. Needles B and C show similar response to the change in air pressure in a lower extent than needles A and D. There is a strong correlation between the needle velocity increase and the pressure increase. The exception to this behavior is needles C and D for which a negligible increase in the velocity is observed when changing from 137.89 to 172.37 kPa (20 to 25 psi).

The average value was calculated in order to obtain the average needle velocity v for each pressure. It is worth noting that needles A and D are located at the far extreme of the tool, while needles B and C are located closer to the tool handle and could serve as an explanation to the similar behavior between the two pairs of needles. The intricacies of the internal mechanisms of the equipment are not part of the scope of this research.

Figure 5.2 shows a comparison between the dynamics of needles A and B for p =137.89 kPa (20 psi). A periodic oscillating pattern can be observed within the recording time $t \in [0, 100]$

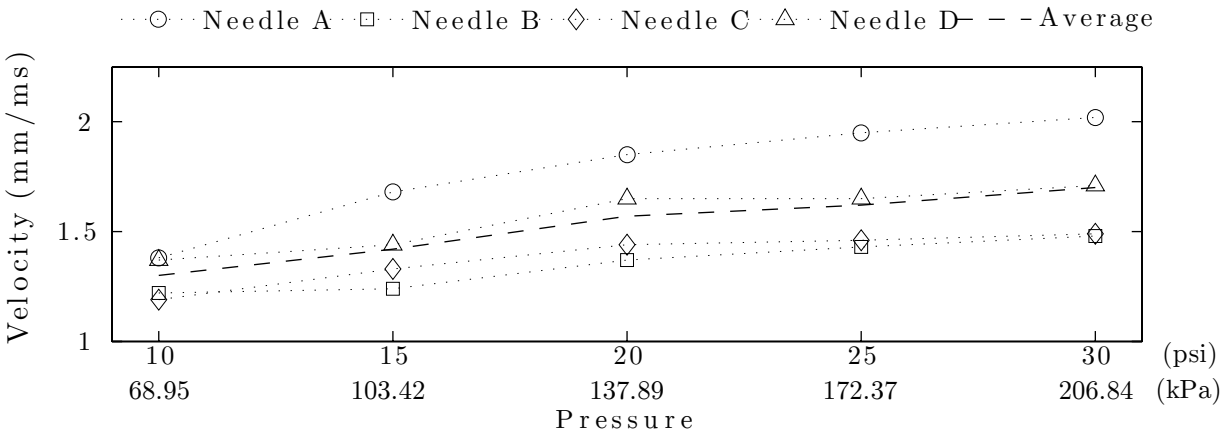

Figure 5.1 Individual needle velocities as a function of air pressure

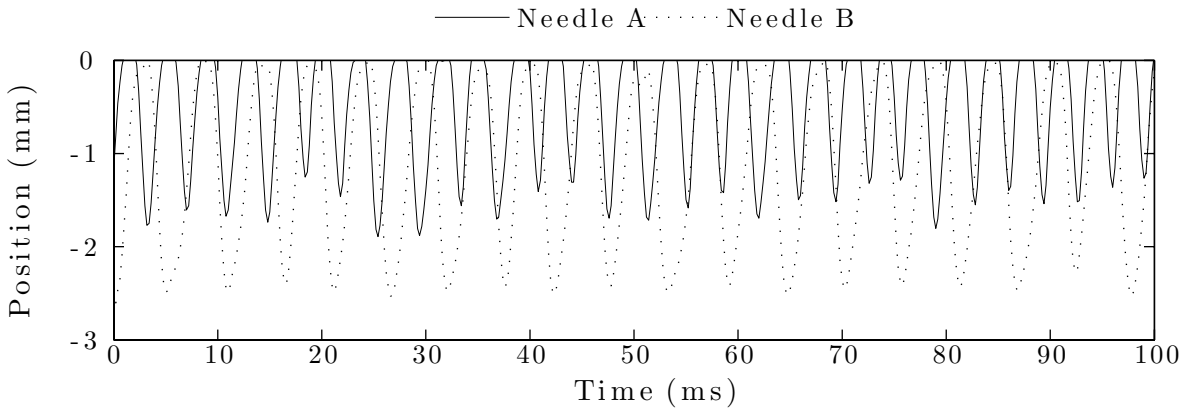

Figure 5.2 Comparison between the dynamics of needles A and B; $p = 68.95$ kPa (10 psi)

ms. This effect is not attributed to the vibration of the tool during operation as vibration was corrected by measuring the needle displacement relative to a reference point. The vertical displacement of needle B is larger; however, the frequency of needle A is higher than that of needle B. This behavior may have an explanation similar to the velocity discrepancies previously explained. Figure 5.3 illustrates the evolution of the frequency of needle A as pressure increases. The frequency in impacts per second was calculated by determining the number of cycles experienced by a needle for $t \in [1, 200]$ ms and extrapolating the result for one (1) second. The relationship between stand-off distance and the impact velocity and frequency was not studied.

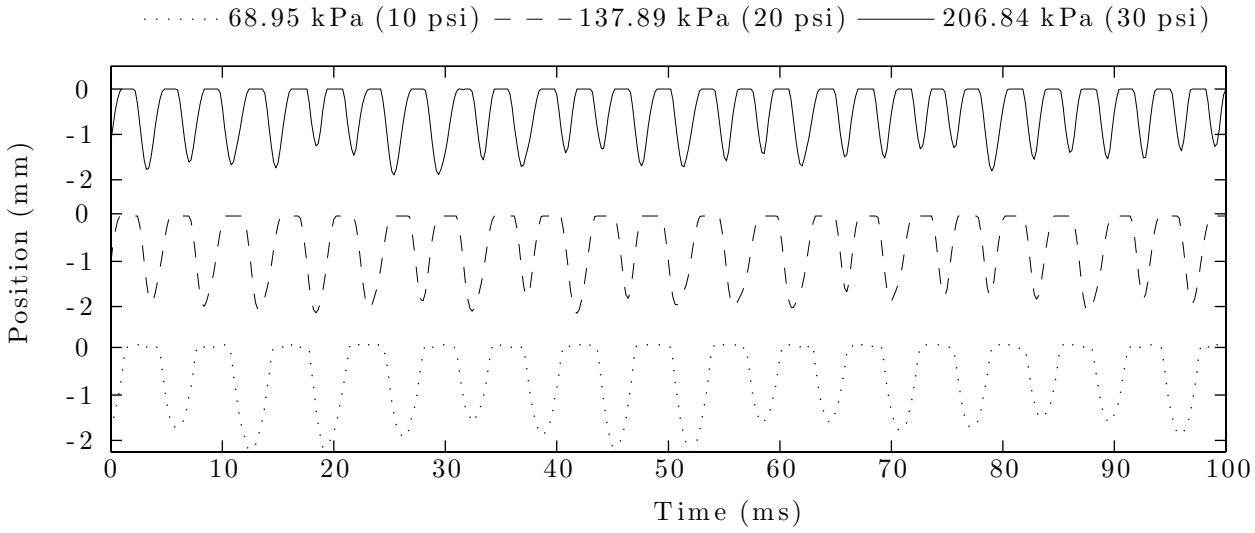

Figure 5.3 Needle tip dynamics progression as a function of air pressure

The impact frequency per needle $f_{i,p}$ obtained from the complete set of needles is presented in Figure 5.4. Similarly to the impact velocity, it is observed that the relationship between the impact frequency and the air pressure is almost linear. If needle velocity increases as pressure increases, and the trajectory is limited by the tool design, it is expected that frequency increases as well. The impact frequency of needles A and D shows an almost identical response to the increase in air pressure. To a lesser extent, needles B and C show an increase in frequency with an increasing air pressure. The difference between the impact frequency of these two subsets is noticeable starting at low air pressure and is maintained throughout the range of values of p. The same grouped behavior noted in the velocity analysis is observed in the case of frequency.

The velocity of needles at impact coupled with their mass is related to the energy of the impacts and therefore to peening. At higher velocities, there is more energy available in the form of kinetic energy to be transferred to the work piece. The frequency of the impacts bears a connection with treatment time and therefore affects coverage development. At higher frequencies, the impact creation rate increases and as a consequence treatment time decreases for the same value of coverage. It is possible to calculate the treatment time requirement for a target coverage value using the Avrami equation for an average indentation diameter $\bar{D}_{\text{ind}}$ in conjunction with the indentation rate, or impact frequency $f_{i,p}$ (Miao et al., 2010). Furthermore, the relationship between air pressure p and the needle velocity v_p and impact frequency $f_{i,p}$ are used to define the initial boundary conditions for the FE model.

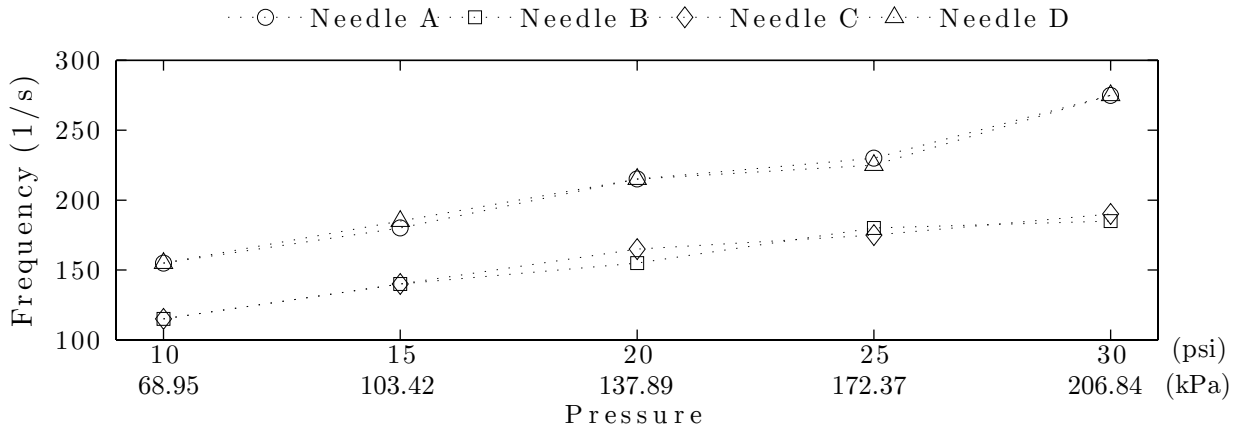

Figure 5.4 Individual needle impact frequencies by air pressure

5.1.2 Experimental procedures

Saturation tests

Thirty-six AA2024-T3 test specimens with similar dimensions to that of an Almen strip and 1.6 mm in thickness were peened using the prototype needle peening equipment. The air pressure was varied for $p = \{68.95, 103.42, 137.89, 172.37, 206.84\}$ kPa ($\{10, 15, 20, 25, 30\}$ psi) to evaluate the relationship between impact speed and intensity. The specimens were peened for treatment times $t = \{30, 60, 120, 240, 480\}$ s.

Figure 5.5 shows the saturation curve that corresponds to $p = 137.89kPa$ (20 psi). Each data point represents the arc height as measured using an Almen gauge after being peened for different treatment peening times t. The initial deflection of the sample was substracted from the measurement to evaluate solely the effects induced by the treatment. The saturation curve as a function of time $Ah(t)$ was generated by performing a non linear least square fit of the form:

$$Ah(t) = q_1(1 - \exp(-q_2 t)) \tag{5.1}$$

where q_1 and q_2 are fitting parameters and t is the treatment time. From the saturation curve it is also possible to calculate the time to reach saturation T_{sat} by determining the lowest value of t upon doubling $(2 \times T)$ results in an arc height increase of 10%; this is obtained through solving for T_{sat} from:

$$Ah(2 \times T_{\text{sat}}) = 1.1 \times Ah(T_{\text{sat}}) \tag{5.2}$$

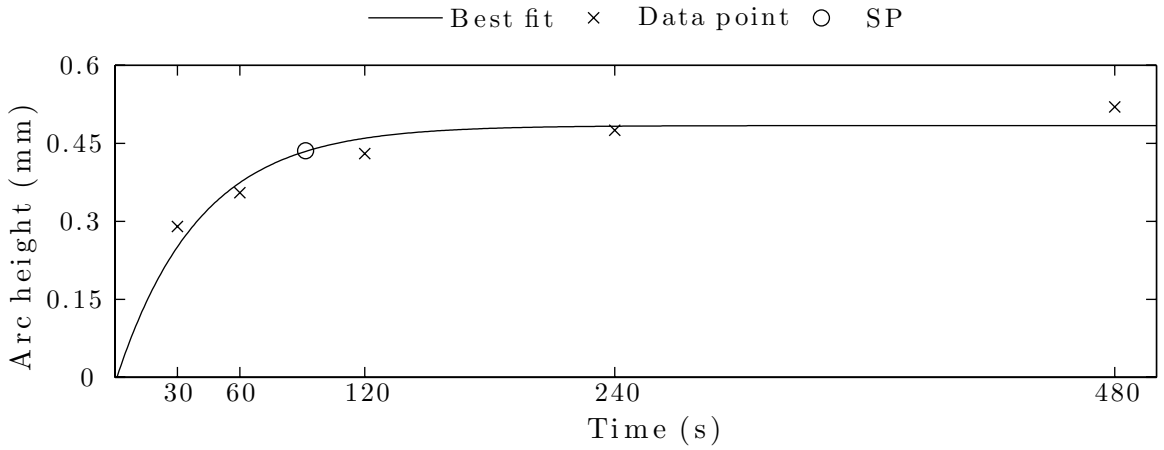

Figure 5.5 Saturation curve for $p = 137.89$ kPa (20 psi)

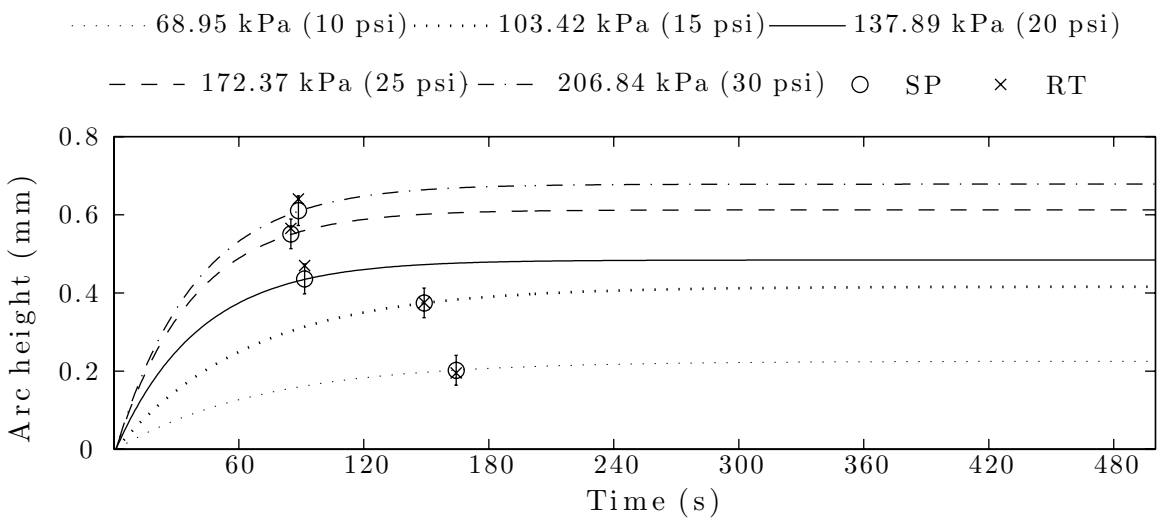

Figure 5.6 Saturation curves for $p = \{68.95, 103.42, 137.89, 172.37, 206.84\}$ kPa ($\{10, 15, 20, 25, 30\}$ psi) using Almen gauge values

The saturation curves for $p = \{68.95, 103.42, 137.89, 172.37, 206.84\}$ kPa ($\{10, 15, 20, 25, 30\}$ psi) and their saturation points (SP) are shown in Figure 5.6. The saturation curves increase in amplitude as the air pressure increases. Similarly, the peening intensity increases with an increasing air pressure almost linearly. As for the saturation time, there is a generally decreasing trend. It is not possible to establish a relationship between air pressure and saturation time with the data points available. A set of test samples were peened at the different saturation times for their corresponding values of p to demonstrate repeatability. The error bars in Figure 5.6 represent the tolerances provided by SAE J443 for one-point intensity verification of a process using the same peening parameters (SAE, 2010); these tolerance values are used to determine the repeatability of a process.

Specimen deflection

The Almen gauge is an accurate tool used to measure the arc height of magnetic test strips after peening. The measurement using a CMM was implemented to reduce the measurement error associated to the incompatibility between the aluminum test samples and the magnetic supports of the Almen gauge. Additionally, the Almen holder measures the radius of curvature in the central portion of the specimen neglecting the effects of peening on the outer bands of the material. The measurements obtained in this section account for total material deflection and therefore the total arc height in the longitudinal and the transverse directions.

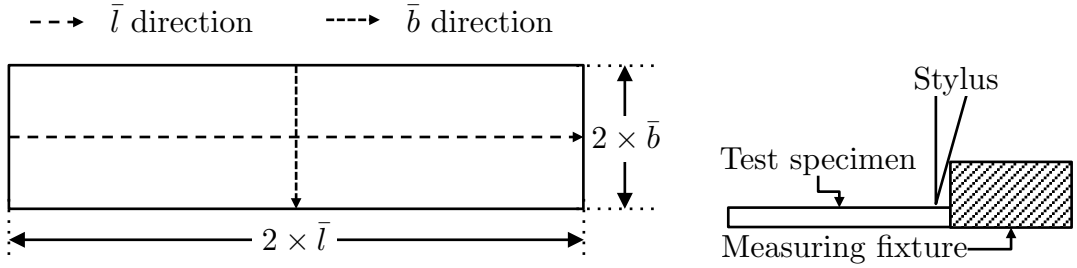

(a) Measuring paths of CMM along the specimen's length $2 \times \bar{l}$ and width $2 \times \bar{b}$

(b) Lateral view of the CMM fixture at the specimen's edge

Figure 5.7 Measuring path and CMM fixture diagram of test specimens

Figure 5.7(a) shows the measuring paths using the CMM where $2 \times \bar{l} = 76$ mm and $2 \times \bar{b} = 19$ mm match the length and width dimensions of the test specimens, respectively. The total profile measurement path along the length and along the width were $2 \times \bar{l}_m = 70$ mm and $2 \times \bar{b}_m = 20$ mm, respectively, due to interference between the measuring stylus and the experiment fixture, as seen in Figure 5.7(b).

Figure 5.8 shows the profile for $p = 137.89$ kPa (20 psi) specimens measured using the CMM for $t = 30, 60, 120, 240, 480$ s and at saturation time. The larger arc and the smaller arc represent the specimens' profiles along their length and their width, respectively. The first data point was obtained from the furthest point from the specimen center along the center line so as to capture the minimum and the maximum points in the profile measurements. The minimum value was substracted from the measured deflection in order to account for

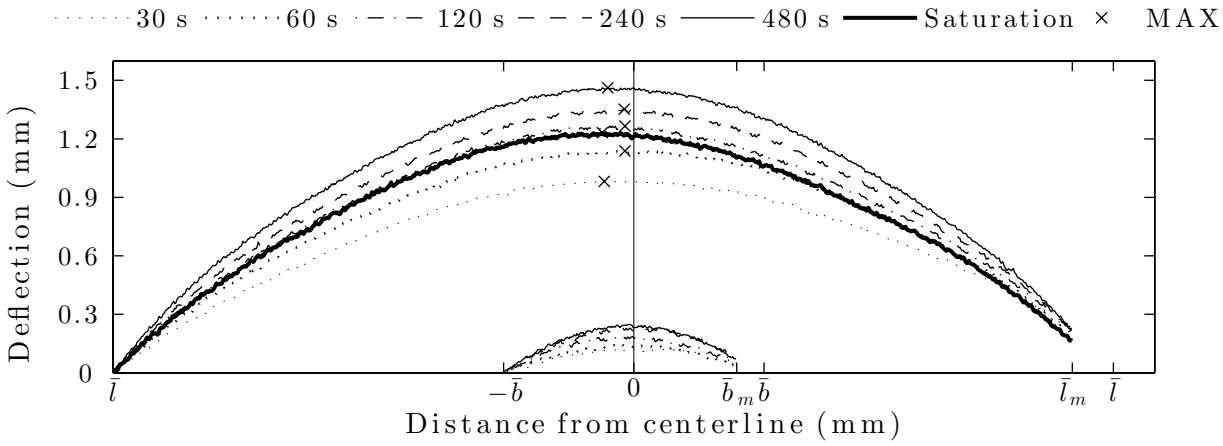

Figure 5.8 Specimen deflection profiles measured by CMM for $p = 137.89$ kPa (20 psi). Specimen length: $2 \times \bar{l}$, specimen width: $2 \times \bar{m}$, measuring path length along the specimen length $2 \times \bar{l}_m$, and measurement path length along the specimen width $2 \times \bar{m}_m$

the specimen's thickness. It was assumed that the specimen's thickness remained constant over the whole process.

A non-linear incremental relationship is observed between peening time and maximum deflection. The amplitude of the deflection observed in the $\bar{l}_m$ directions is greater than that in the $\bar{b}_m$ direction. These results are consistent with other peening processes. The maximum deflection (MAX) is expected to occur at the center of the specimen. The results obtained show a misalignment. This is attributed to the fact that the treatment needs to be perfectly uniform for the deflection to be perfectly aligned and manual methods cannot be controlled to that extent. In addition, the peening trajectory could have influenced the resulting peening shape leading to the asymmetry observed in the longitudinal direction (Gariépy et al., 2013). The roughness observed in the deflection profiles is attributed to the plastic deformation of the peened surface induced by the repeated impacts.

Figure 5.9 shows a comparison between the saturation curves generated from the deflections using the CMM and the Almen gauge for $p = 137.89$ kPa (20 psi). The results in the length's direction resemble the behavior observed during the intensity verification when the arc height was measured using the Almen gauge. However, the measurements obtained using the CMM are greater than those obtained using the Almen gauge since the latter only measures the deflection in a segment of the arc. The saturation times for the complete arc height differ from those obtained previously. The saturation point obtained for the arc segment using the Almen holder only measure changes in the central portion of the component making the saturation point more sensitive to smaller variations in individual arc heights. The CMM values are corrected by measuring the deflection of the specimens' central region that mimic the gap

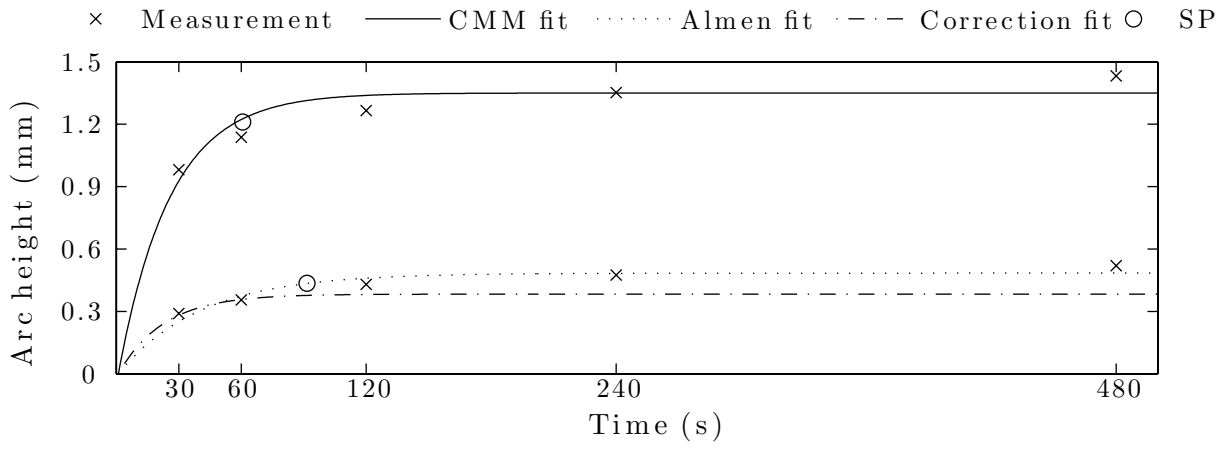

Figure 5.9 Arc height and saturation curve comparison between the deflection measurements using the Almen gauge and the CMM

Table 5.1 Relationship between peening pressure and measured arc height at saturation AH_s^m

Pressure (kPa)	$AH_{\text{Sat}}^{\text{cmm}}$ (mm)	$T_{\text{Sat}}^{\text{cmm}}$ (s)	$AH_{\text{Sat}}^{\text{Almen}}$ (mm)	$T_{\text{Sat}}^{\text{Almen}}$ (s)
68.95	0.6492	146.40	0.2027	164.33
103.42	1.1100	108.35	0.3743	148.93
137.89	1.2197	60.68	0.4356	91.57
172.37	1.5337	64.55	0.5510	85.01
206.84	1.6704	62.93	0.6103	88.55

between the fastening screws of the Almen holder (≈ 40 mm). The corrected conversion and the Almen fits show close resemblance; it is therefore convenient to use the deflection values obtained by CMM for the rest of the study.

Figure 5.10 shows the saturation curves for $p = \{68.95, 103.42, 137.89, 172.37, 206.84\}$ kPa ($\{10, 15, 20, 25, 30\}$ psi) for the CMM measurements. The arc height increases for higher pressure values. The re-test (RT) arc height measurements are provided for reference only. While in close agreement, the tolerances to determine repeatibility are not applicable in this case since the method and the equipment to measure the deflection are not the same as those used in SAE J443. The deflection values obtained at the saturation points can be used as a reference in order to assess the adequacy of the prediction of needle peening results by means of numerical methods. Table 5.1 summarizes the results obtained from the specimen deflection experimental analysis. The peening times at saturation are compared, for all pressures. As expected, it is observed an incremental trend in the deflection at saturation as

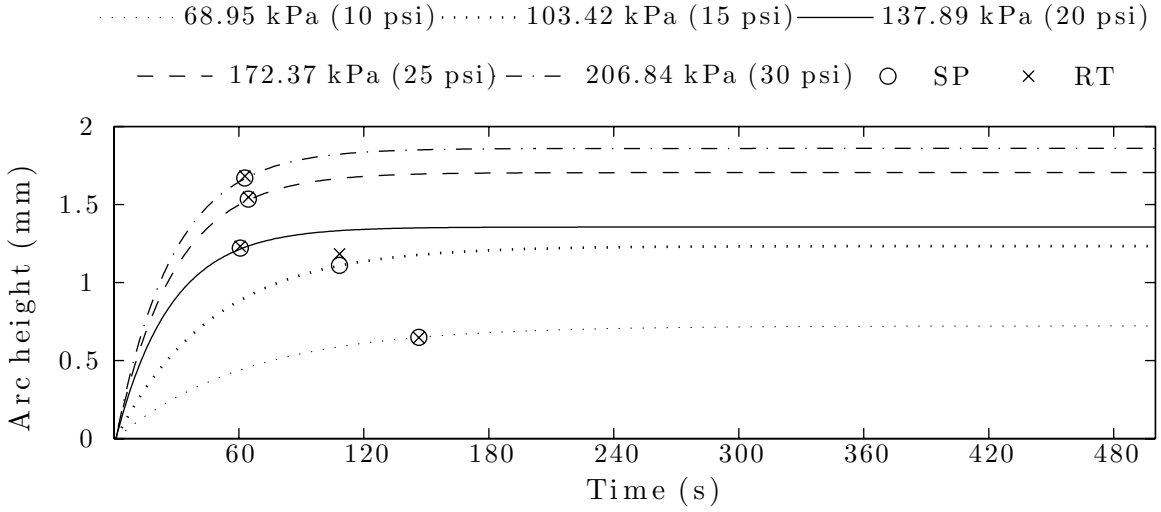

Figure 5.10 Saturation curves for $p = \{68.95, 103.42, 137.89, 172.37, 206.84\}$ kPa ($\{10, 15, 20, 25, 30\}$ psi) using CMM values

pressure increases, for both methods. However, it is not possible to establish a behaviour in the evolution of the saturation time.

Indentation analysis

A study of the shape and size of the impact indentations for different peening pressures p was performed. A magnification of $\times 100$ was used to obtain a general appreciation of the indentations distribution, while a magnification of $\times 200$ was used to accurately measure the indentations. Samples with low coverage were selected to obtain a better view of isolated dents.

Figure 5.11 shows the magnified surface images for a sample peened at $p = 137.89$ kPa (20 psi) for $t = 60$ s. Figure 5.11(a) shows the general shape and distribution of the indentations using a $\times 100$ optical magnification. The indentations are circular in shape and of different sizes. The brighter region at the center of the indentations represent the deepest part of the indentation which reflects the light from the camera. Since the impacts are normal to the surface it was expected that the pocket would be centered. The dark spot seen in Figure 5.11(a) was determined to be a surface defect.

Figure 5.11(b) shows a $\times 200$ magnification of the white rectangle shown in Figure 5.11(a), as well as the measured indentation diameter. This magnification allows for measuring the smallest (d^s_{20}) and largest (d^l_{20}) indentation diameters by approximating them as perfect circles. The diameters obtained after digital analysis were of $d^s_{20} = 0.1628$ mm and $d^l_{20} =$

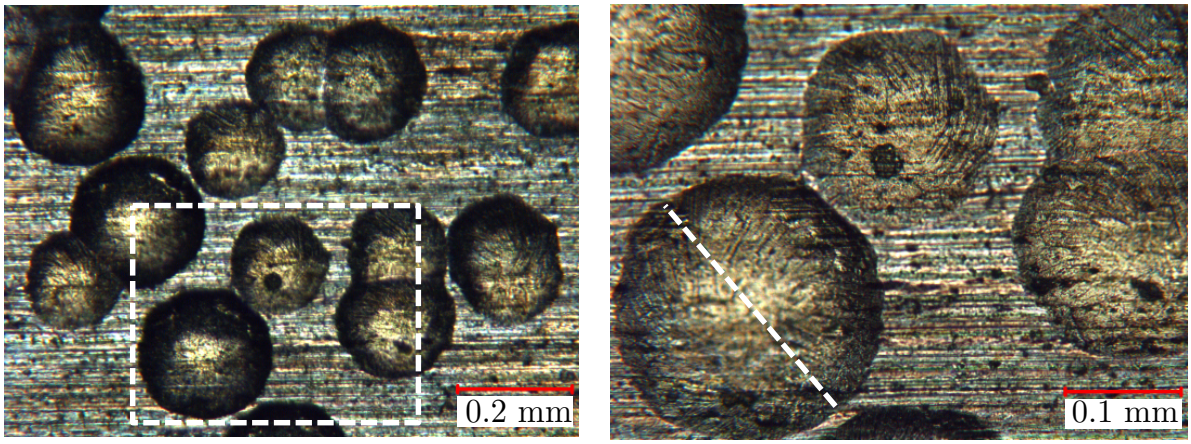

(a) $\times 100$ magnification (b) $\times 200$ magnification

Figure 5.11 Microscopic photography of indentations of test sample peened at $p = 137.89$ kPa (20 psi)

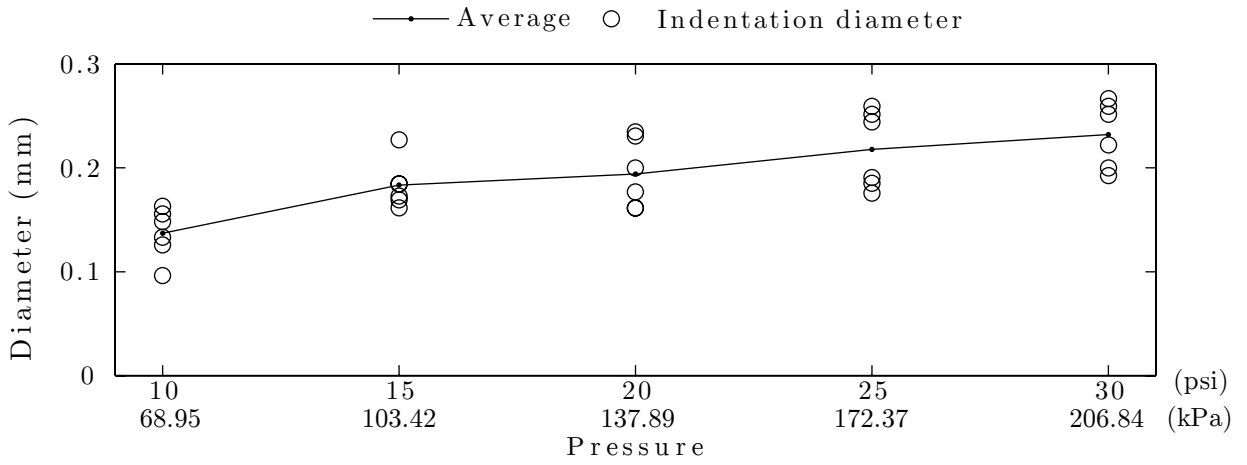

Figure 5.12 Sampled indentation diameters and average size for $p = \{68.95, 103.42, 137.89, 172.37, 206.84\}$ kPa ($\{10, 15, 20, 25, 30\}$ psi)

0.2222 mm, respectively. The areas of the indentations are then $A^s_{20} = 0.0208$ mm^2 and $A^l_{20} = 0.0387$ mm^2. This means that the smallest indentation produces a coverage per impact 57.75% smaller than the largest. This difference was attributed to the variations in impact velocities among the different needles, as presented in Section 5.1.1. The higher the velocity, the higher the impact energy is; therefore, higher impact energy translates into larger indentations. The indentation area variation may have implications in the coverage and therefore in treatment time.

A distribution of indentation diameters randomly sampled from images similar to Figure 5.11 for the range of air pressures p is presented in Figure 5.12. There is an almost linear relationship between air pressure, which in turn makes a direct relationship between impact velocity and indentation diameter.

Residual stress determination

The test strip peened at $p = 137.89$ kPa (20 psi) for saturation was destructively tested in order to obtain the through-thickness residual stresses using the XRD technique. Figure 5.13 shows the residual stress values as a function of z. The distribution of residual stresses σ_{res} is obtained using these points. The test sample was released from its physical constraints, and therefore found in its balanced state. This means the measured stresses correspond to the residual stresses as opposed to the stresses directly induced by peening. For $z > 0.6$ mm, the residual stress profile was calculated as to obtain $\int_0^h \sigma_{res}(z)dz = 0$ by assuming a linearly decreasing slope to replicate a stress profile that meets the criteria of Equation 2.4

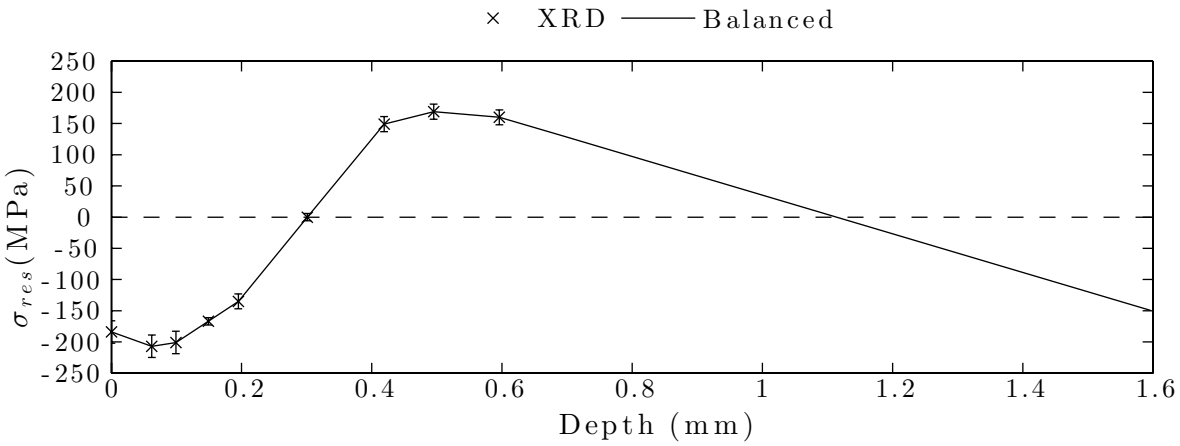

Figure 5.13 Residual stresses σ_{res} profile on an AA2024-T3 strip peened at $p = 137.89$ kPa (20 psi)

Figure 5.13 reveals that peening produces compressive residual stresses (negative in sign) at the surface. The maximum stress in compression is found underneath the surface at $z = 0.062$ mm, while tensile stresses are observed in the sample's core. It is observed that for $z \simeq 0.5$ mm, which corresponds to the maximum tensile stress value, the residual stresses tend to decrease. This trend is consistent with typical peening stresses (Miao et al., 2009).

It must be pointed out that the time lapse between the sample's peening and the residual stress measurement was greater than 60 days, and it was assumed that no stress relaxation occurred over that period. Moreover, it is assumed that the residual stress measuring method did not induce stresses that significantly affected the peening-induced residual stress profile.

5.2 Numerical analysis

5.2.1 FE impact model - single impact

Convergence analysis

A convergence analysis was performed to determine the appropriate mesh density for $N = 1$ impact at $v = 2.5$ mm/ms. These conditions were chosen as it was expected that they would deliver the most severe deformations. It was hypothesized that simulations for lower energy impacts should converge for the same mesh density as those for higher energy. The element size was determined as a function of the needle tip radius R_n. Figure 5.14 shows the induced stress profiles after a single impact for the $R_n/10$ (Gariépy et al., 2011) and $R_n/15$ mesh densities.

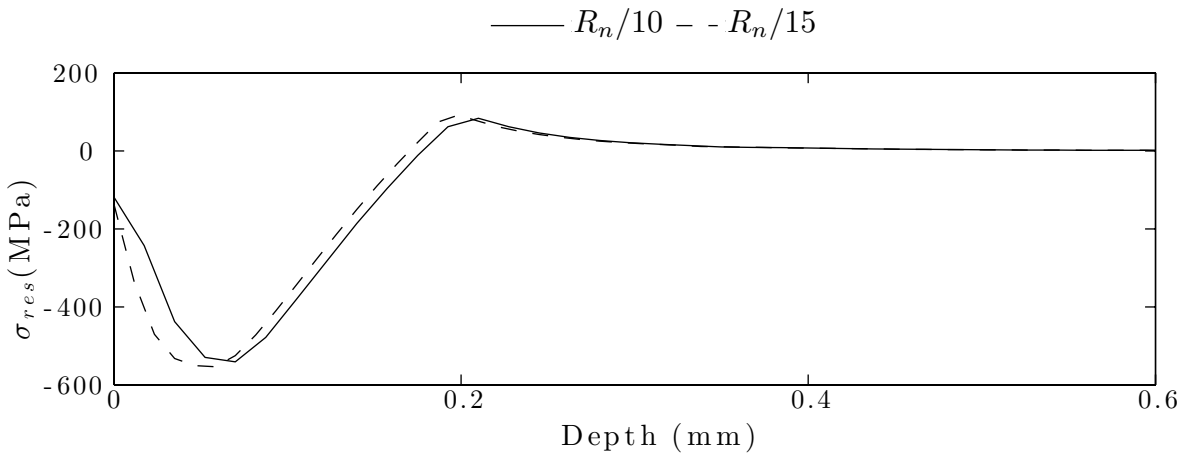

Figure 5.14 Convergence analysis between $R_n/10$ (Gariépy et al., 2011) and $R_n/15$

The calculation time for the model having elements of sizes $R_n/10$ was 28 minutes and for that of $R_n/15$ was of 121 minutes. The Figure reveals that there is no significant difference between the surface residual stresses predicted by both mesh densities, while the difference between the maximum compressive stress and the maximum tensile stress are 2% and 8%, respectively. Based on the similarity of results and the computation efficiency, the mesh $R_n/10$ was selected for the remaining simulations.

Indentation diameter prediction

Single impact analysis was also used to estimate the indentation diameter. Figure 5.15 shows the displacement field along the Z-axis, U_z, of the surface nodes for $Z = 0$ and $Y = 0$ after one impact at $v = 1.57$ mm/ms. The indentation diameter was obtained by measuring the distance between the two intersecting points of the node line and $Z = 0$, which represents the part's surface. It is observed that the predicted diameter (D_{prd}) obtained from the single impact simulation is within the minimum (D_{min}) and maximum (D_{max}) limits determined by the indentations experimental measurements. Material build-up was observed

Table 5.2 Relationship between air pressure and impact velocity

Air pressure (psi)	Air pressure (kPa)	Impact velocity (mm/ms)
10	68.95	1.30
15	103.42	1.42
20	137.89	1.57
25	172.37	1.62
30	206.84	1.70

Table 5.3 Measured and predicted indentation diameters after single impact

Velocity (mm/ms)	Lower limit (mm)	Upper limit (mm)	Predicted (mm)
1.30	0.0963	0.1630	0.1862
1.42	0.1615	0.2269	0.2182
1.57	0.1612	0.2346	0.2271
1.62	0.1756	0.2593	0.2314
1.70	0.1926	0.2667	0.2344

surrounding the indentation but was not taken into account for measuring the indentation diameter. The reason for this is that the material build-up could hardly be discriminated from visual inspection (see Section 5.1.2). A robust method for measuring indentation sizes and coverage is yet to be developed. The impact diameter comparison between the experimental and predicted results demonstrates the adequacy of the model parameters selected and the behavior determined by the equipment characterization.

Single impact simulations were performed for the remainder of the needle velocities studied and the diameter of the indentation was determined using the same criteria. Table 5.3 shows the comparison between the measured and predicted indentation diameters after a single impact simulation. The lower and upper limits indicated in the table were determined by the smallest and largest diameters measured experimentally, for each pressure level. The predicted indentation diameters are consistent with the experimental values, showing the capability of the model to predict the response of AA2024-T3 after a single impact with the exception of the lowest velocities studied, which showed a deviation of 14%.

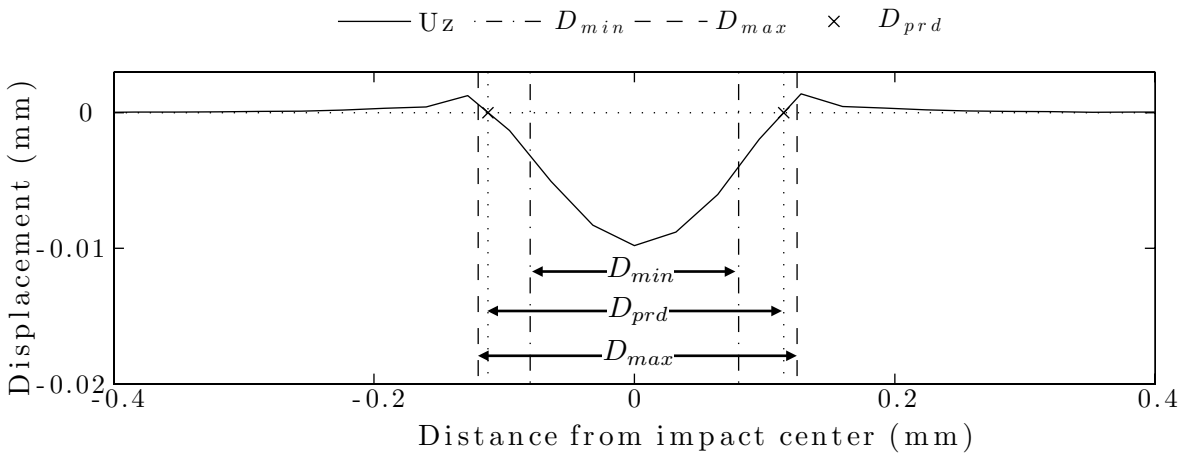

Figure 5.15 Surface nodes U_Z after single impact for $v = 1.57$ mm/ms

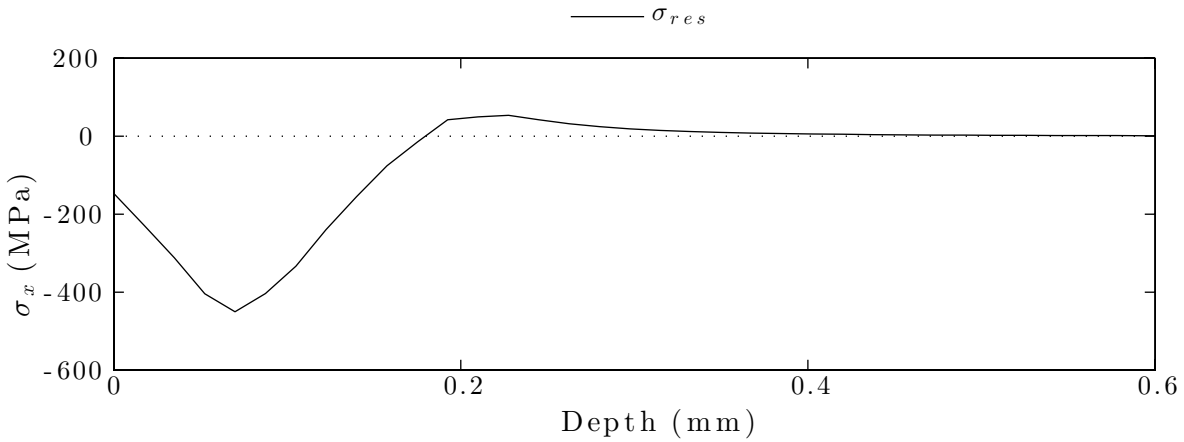

Figure 5.16 Stresses in the X-direction measured under the impact point for $v = 1.57$ mm/ms after a single impact

Single impact residual stress

Through-thickness residual stresses calculation under the impact point's center at $v = 1.57$ mm/ms is shown in Figure 5.16. On the surface ($z = 0$ mm), the residual stress is compressive, denoted by the negative (-) sign. The maximum compressive stress is found underneath the surface. Deeper into the material the stresses become tensile; the maximum tensile stress is lower than the maximum compressive stress in its absolute. The stresses converge to zero as the material depth increases. The resulting profile is consistent with the typical profile obtained after single impact shot peening simulations.

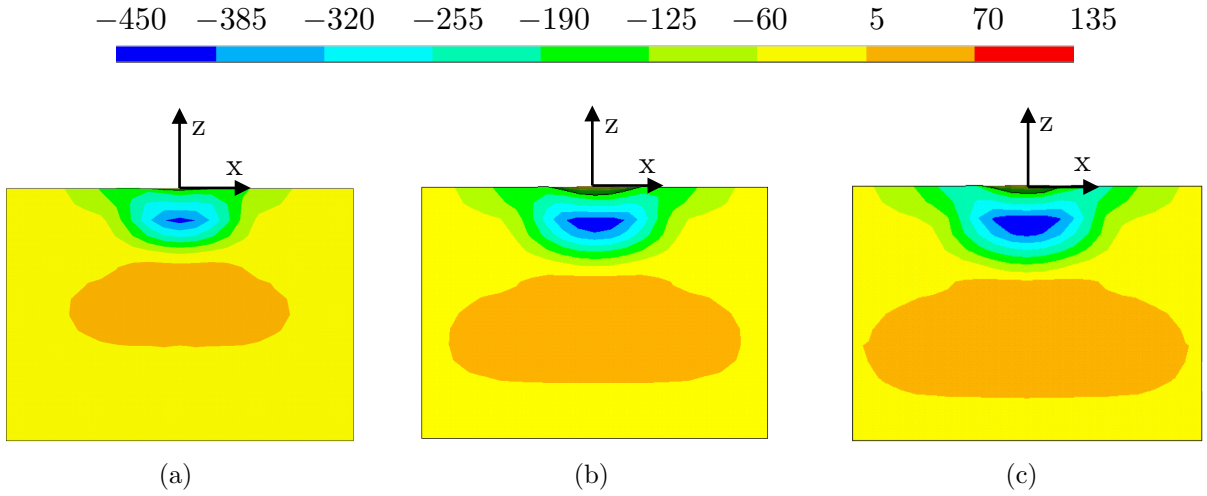

Figure 5.17 Cross-section induced stresses (MPa) contour plot after single impact for (a) $v = 1.30$ mm/ms, (b) $v = 1.57$ mm/ms and (c) $v = 1.70$ mm/ms

The material response in terms of induced stress fields was studied for different impact velocities. Figure 5.17 shows the cross-sections ($X = [-0.4, 0.4]$, $Y = 0$ and $Z = [0, -0.6]$) of the impact point (centered on $X = Y = 0$) and the surrounding material for $v_{=}\{1.30, 1.57, 1.70\}$ mm/ms. The scaling factor of plots was set to $DS = 2$ in the post-processing result viewer for a better appreciation of the surface deformation. The same contour plot value limits were established for the three cases.

The plastic deformation difference at the impact point between the three scenarios is obvious. The diameter of the indentation increases with an increasing v, which is consistent with the results presented in Table 5.3. It is observed that the penetration depth shows the same incremental trend in relation to v. The maximum compressive stress is found underneath the surface aligned with the impact point and its print increases for higher energy impacts.

The compressive and the tensile stresses introduced by the impact increase in magnitude and extension as v increases, with a difference in the maximum compressive stress of 5% between $v = 1.30$ mm/ms and $v = 1.70$ mm/ms. However, the induced stress field increased its footprint by 35% from $v = 1.30$ mm/ms to $v = 1.70$ mm/ms. The fact that sub-surface stresses extend further than the surface indentation suggests that equivalent peening results may be obtained when approaching 100% coverage. Since coverage is used as a primary peening monitoring parameter in the industry, a study relating the surface coverage to the material's internal state is recommended for future research.

5.2.2 FE impact model - multiple impacts

Figure 5.18 shows the average induced stress profiles calculated with a 1.6 mm thick impact model for $N = \{10, 20, 40, 80, 160, 320\}$ randomly located impacts for a velocity $v = 1.57$ mm/ms. The calculation time as a function of impact numbers N is shown in Figure 5.19. The stress profiles were obtained by averaging the nodal solution of σ_x of the nodes in region 4 (see Figure 4.6(c)) as a function of the depth z. It was noted that the stresses in the X and Y-directions were almost identical and therefore only the X direction was considered.

It can be seen from Figure 5.18 that the depth of compressive residual stresses increases with the number of impacts. In addition, the surface stress magnitude, the maximum compressive stress in the near-surface and the maximum tensile stress deeper in the material increase. The depth at which the maximum compressive is found does not increase significantly, being located at around 0.08 mm inside the target. It can also be seen that as N approaches its greatest value, the degree of change in the stress profile is less noticeable, which suggests that the material converges towards saturation.

Figure 5.20 shows the saturation curve generated with the FE forming model using the predicted average induced stresses as input. Given that the impact locations were generated randomly, it was suspected that the average induced stresses would be influenced by the impact distribution. In order to account for the stochastic nature of the simulation, five repetitions were run for each value of N with different impact coordinates. The data was fitted according to:

$$Ah(N) = \frac{c_1 N^2 + c_2 N}{c_3 + N} \tag{5.3}$$

where c_1, c_2 and c_3 are fitting parameters.

The regression was fitted using the least square differential scheme through the 30 simulated arc height values. The solution was obtained with a regression coefficient $R^2 = 98.23$ and a confidence interval $CI = 95\%$. Table 5.4 lists the fitting parameters and the saturation point predicted for $v = 1.57$ mm/ms. The saturation point was obtained with the criteria $Ah(2N) = 1.1 \times Ah(N)$, as for the experimental data. The number of impacts at saturation N_{sat} was rounded to the next whole number as fractions of impacts are not possible. The saturation was found to occur at $N = 137$ impacts with a resulting specimen deflection of $Ah_{sat} = 1.24$ mm. Therefore the model developed predicts that the studied sample reaches its saturation point after $N = 137$ impacts according to the definition of Almen intensity.

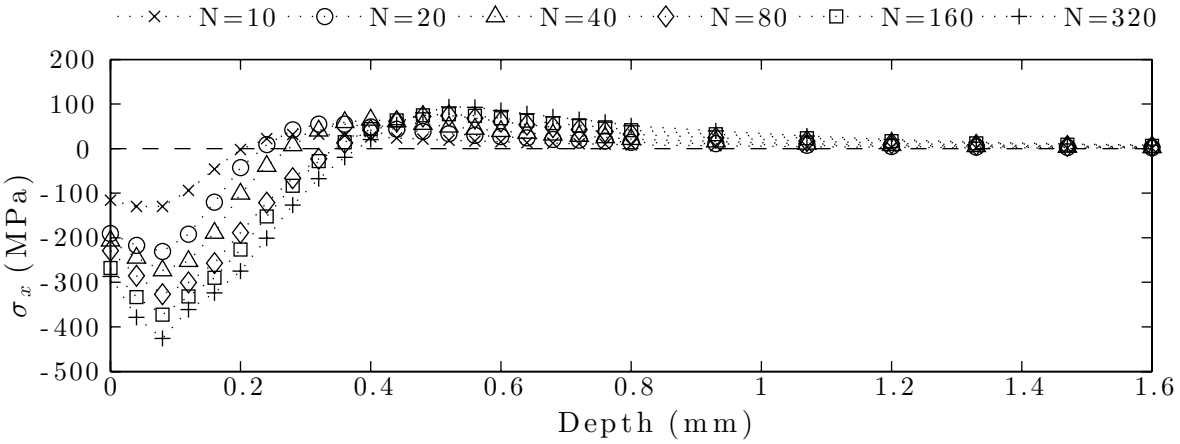

Figure 5.18 Average induced stress: $N = \{10, 20, 40, 80, 160, 320\}$, $v = 1.57$ mm/ms

Table 5.4 Arc height saturation solution for $v = 1.57$ mm/ms

Fitting parameter c_1	Fitting parameter c_2	Fitting parameter c_3	N_{Sat}	Ah_{Sat} (mm)
-2.93×10^{-4}	1.772	64.54	137	1.24

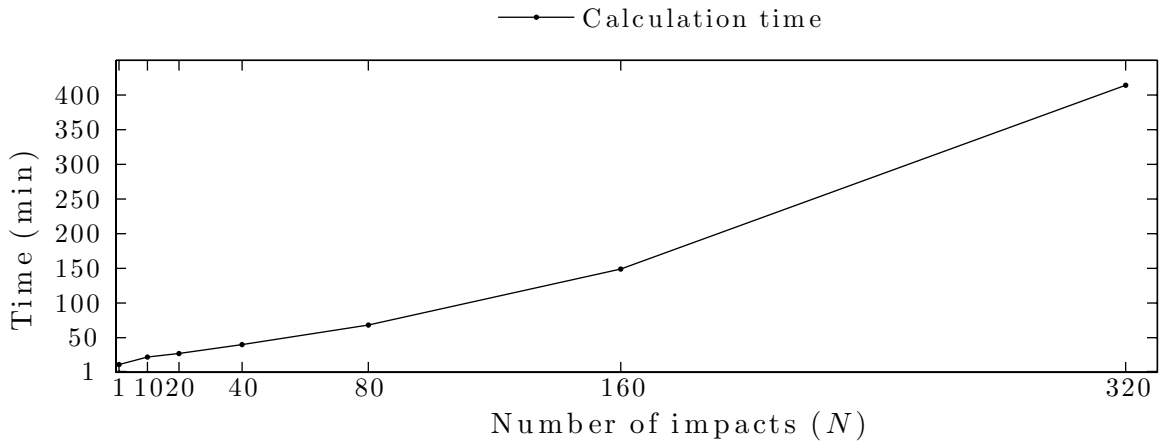

Figure 5.19 Simulation calculation time: $N = \{10, 20, 40, 80, 160, 320\}$, $v = 1.57$ mm/ms

An additional FE simulation was performed in order to determine the induced stress profile after peening to the saturation point. Figure 5.21 shows the induced stress profile for $N = 137$ and $v = 1.57$ mm/ms. The residual stress distribution was calculated from the averaged induced stress at saturation by adding the axial and bending stresses experienced once the component is released from its boundary conditions. The relationship between residual, induced, bending and stretching (or axial) stresses is also shown in Figure 5.21. It is important to note that the residual stress profile remains compressive in the surface; this results is of utmost importance as it is the compressive residual stresses that are related to the improvements in fatigue life of peened components.

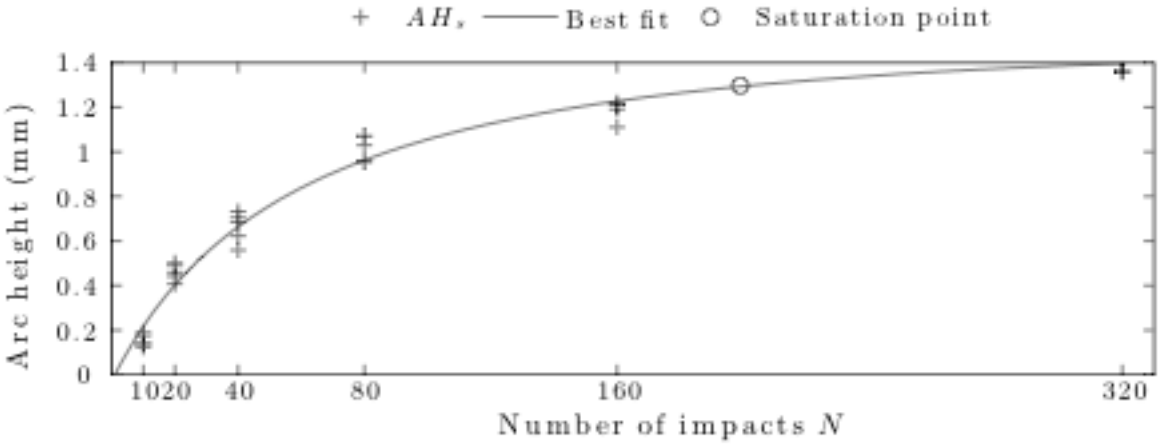

Figure 5.20 Simulated arc heights and fitted saturation curve for $v = 1.57$ mm/ms

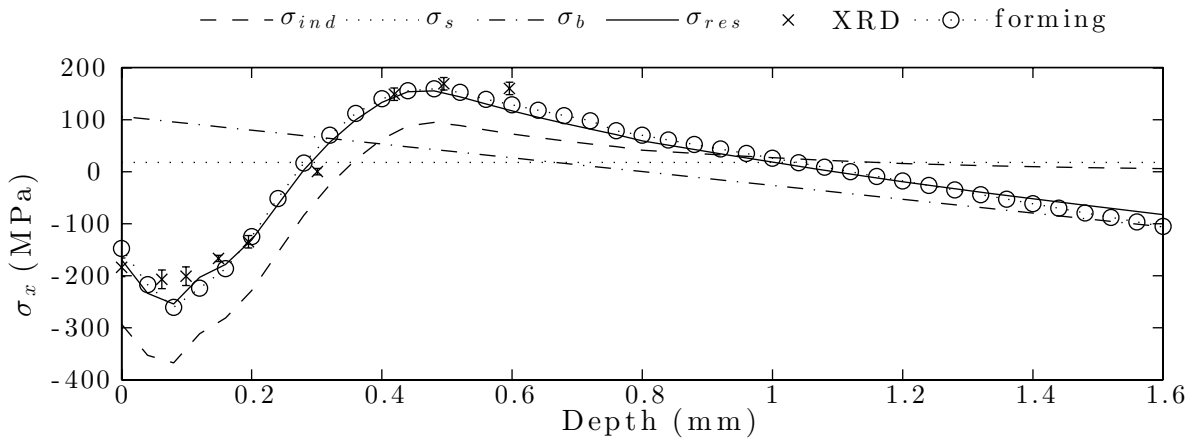

Figure 5.21 Residual stress balancing for saturation of $v = 1.57$ mm/ms and comparison with experimental results

The model results were compared against the residual stress profile obtained experimentally in order to produce a definitive validation of the modeling and predictive methodologies. It was decided to validate the model using the residual stress development as opposed to comparing only the arc heights. It is suspected that two different stress profiles can produce the same arc heights. In the same note, validating the development of residual stresses by comparing the predicted results against the experimental determinations would predict the resultant material deformation produced as a consequence of the induced stresses.

Figure 5.21 shows the comparison between the balanced residual stress profile predicted after $N = 137$ impacts at $v = 1.57$ mm/ms using the random multiple impact model and the residual stresses determined experimentally by the XRD method. Overall, there is good accordance between the predicted and experimental results. The surface residual stress and the tensile stress in the material are accurately predicted. Additionally, the residual stress profile obtained as a result of the material deflection from the peen forming model is compared against the solution of the balanced stress profile obtained from the induced stresses. Both profiles are in close resemblance to the experimental results.

Figure 5.22 shows the stress and plastic strain fields in the cross-sections taken at $X \in [-0.4, 0.4]$, $Y = 0$ and $Z \in [0, -0.6]$. It is observed that the plastic strain decreases rapidly further away from the area subject to impacts, as seen in Figure 5.22(b). Since strain amplitudes influence the yield stresses stabilization, a model that considers the fact that the material closer to the surface experiences higher strain amplitudes might improve the results. The model developed by Zimmermann et al. (2010) contemplated these variations in the FE modeling of shot peening of IN718.

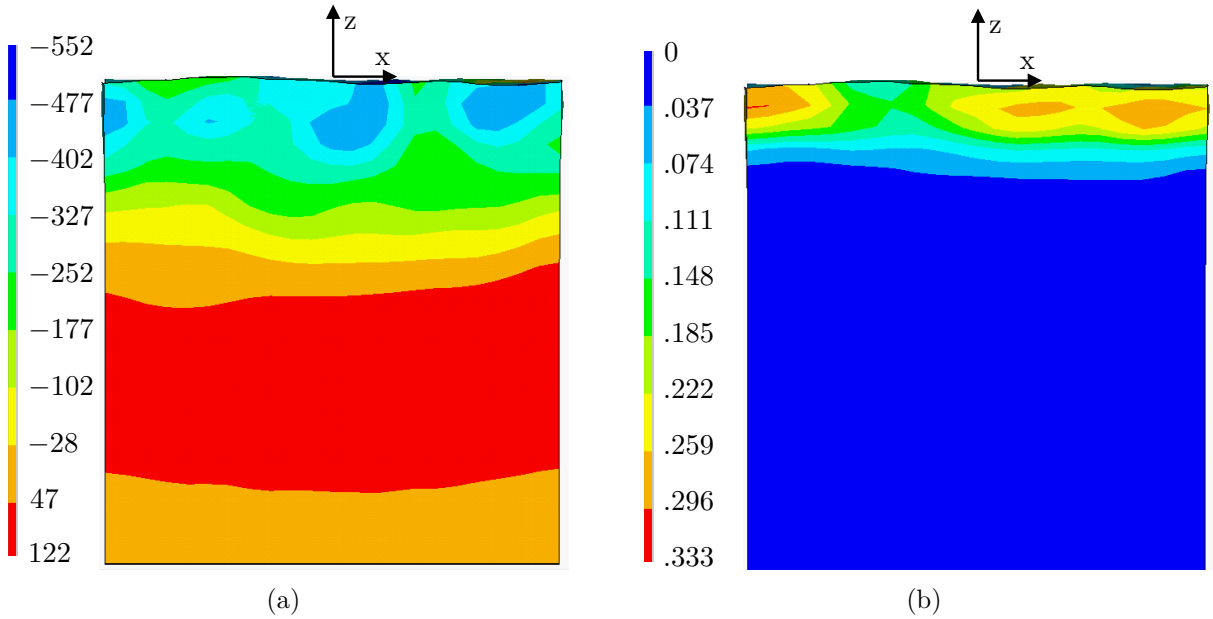

Figure 5.22 Cross-section, internal state of the material at saturation for $v = 1.57$ mm/ms. (a) Induced stresses σ_x in MPa; (b) von Mises plastic strain

The confidence gained from the model validation using the XRD results allowed to compare the measured specimen deformation at saturation against the deflection measured using the CMM. Needle impact velocities $v = \{1.30, 1.42, 1.62, 1.70\}$ mm/ms were also studied in addition to $v = 1.57$ mm/ms. Similarly to case of $v = 1.57$ mm/ms, numerous impact simulations were executed for each impact velocity by varying the number of impacts N to construct a saturation curve that best fitted through the 30 data points using a regression that employed the least square differential scheme, as for the case of $v = 1.57$ mm/ms. The comparison is presented in Table 5.5; $Ah_{\text{Sat}}^{\text{cmm}}$ is the arc height measured at saturation with the CMM, Ah_{sat}^{p} is the predicted arc height at saturation using the FE models and N_{sat}^{p} is the predicted number of impacts to achieve saturation. For $v = 1.42$ mm/ms and $v = 1.57$ mm/ms, the model was capable of predicting accurately the arc heights; this was expected

Table 5.5 Predicted and measured arc height comparison

Velocity (mm/ms)	$Ah_{\text{Sat}}^{\text{cmm}}$ (mm)	Ah_{sat}^{p} (mm)	N_{sat}^{p}	$\Delta(\%)$
1.30	0.65	0.9812	147	+50
1.42	1.11	1.1104	116	+0.3
1.57	1.21	1.2432	137	+2.4
1.62	1.53	1.3642	152	-11.1
1.70	1.67	1.4464	131	-13.2

for the latter given the close resemblance between the predicted and the measured residual stresses. A possible explanation for the underestimation of some results is that the model boundary conditions did not allow the sample to arc gradually while being peened, which lead to smaller radius of curvature (or larger arc height), as explained by Zimmermann et al. (2008). In the case of $v = 1.30$ mm/ms, the overestimation of the arc height can be explained by the fact that the indentation diameter predicted by a single impact was larger that the measured value. The underestimation of the deflection could be attributed to the fact that the initial stresses take more influence for lower peening intensities; further investigation is required. However, given the similarity of the prediction to the measured values, these were considered relevant. In addition, taking into account the forming stresses from rolling the material into the final form could potentially help improving the arc height prediction.

The effect of model thickness was evaluated by using the same material properties samples of different thickness. The target thickness studied were 1.6 mm and 3 mm. The maximum difference in average induced stress was negligible (<3%). It was determined that this difference did not affect the sample arching. The model developed in this study can be used to predict the internal stresses of the material for different sheet thicknesses. The effect of model thickness for sheets thinner than 1.6 mm was not studied; therefore this recommendation holds only for thicker targets.

CHAPITRE 6 GENERAL DISCUSSION

This study has allowed to predict the induced stress profile and the consequent material deformation of thin aluminum strips subjected to needle peening. To achieve this, the equipment was studied under high-speed scenarios in order to quantify its dynamics. These values were used as initial boundary conditions to simulate, using the FE method, the dynamic impacts characteristic of needle peening. This model allowed to calculate the induced stresses by the process for different treatment parameters. The response of the material in terms of induced stresses varied with the change in impact velocity by showing profile stresses larger in magnitude and in depth at higher velocities. The predicted residual stresses were then used in a peen forming model to calculate the material deflection. The model was capable of predicting the material deformation for a range of working pressures. This was validated by the accordance between the predicted induced stress profile at saturation and that measured experimentally with the XRD method.

It was observed from the equipment characterization campaign that, as working pressure increases, the impact velocity increases in an almost linear relationship. There was a difference in the individual needle velocities observed that became more evident at higher pressures. Similarly, there was an increasing, almost linear, relationship between pressure and impact frequency, as well as a difference in the individual needle frequencies that became more evident at higher pressures. The needles that showed a lower than average impact velocity are the same that showed a lower impact frequency. This remark is of relevance since it was assumed in the model that all needles contributed equally to the peening. Therefore, the effect of the low energy bearing needles might have been underestimated.

The development of the saturation curves using the Almen holder and the CMM showed that the intensity increases at higher pressures. This was an expected response as the amount of induced plastic deformation increased for more energetic impacts. This was furtherly validated with the indentation analysis. It was not, however, possible to establish a trend between the working pressure and the saturation time. Regardless, it was possible to demonstrate the repeatablity of the process by obtaining very similar deflection measurements of specimens peened for the calculated saturation times.

It was observed that for the same working pressure, the indentations created by the needles varied in diameter. This was naturally expected as behavioural variation between the needles was shown during the equipment characterization. Despite the fact that the diameters were measured using high magnification factors, the determination of the plastically deformed

area is challenging to assess visually. The single impact FE analysis was capable of predicting the indentation diameters for the cases of $p = \{103.42, 137.89, 172.37, and 206.84\}$ kPa $(15, 20, 25, 30$ psi); it was observed that at higher pressures the predicted value tends towards the upper limit of the measured values. However this was not the case for $p = 68.95$ kPa (10 psi); an overestimation by 14% was observed. This overestimation might be an explanation to the discrepancy between the predicted and the measured arc height for $p = 68.95$ kPa (10 psi).

The underestimation of the arc height at higher working pressures might be explained by the fact that the differences in the behaviour among the needles is accentuated at higher values of p. This was oberved in the velocity, the frequency and the variation of the impact diameters measured using microscopic photography. Since the model used the average of the impact velocity as an initial boundary condition, it may be that this average value was less representative of the actual velocity for higher pressures. Additionally, the impact model does not allow for the target to progressively deform as it is impacted, which could have resulted in an underestimation of induced stresses and deformation (Zimmermann et al., 2008). This difference could be explained more accurately by comparing the predicted results to experimental XRD profiles.

CHAPITRE 7 CONCLUSION

This Master's research project had as a general goal to predict the performance of a needle peening equipment prototype in the frame of a parternship with a local Quebec developer of peening solutions. The goal of this thesis was to predict the effects of needle peening using the mentioned equipment on AA2024-T3 sheets by incorporating existing modeling techniques developed for shot peening. The purpose was to provide the equipment developer with numerical tools that are robust enough to be used as part of the design and optimization cycle of the product, as well as to set the foundation for the characterization and modeling of peening methods alternative to shot peening. The principal conclusions of this study are:

- The needle peening tool, the SPIKER^{TM}, is capable of being characterized by a combination of high-speed photography and numerical algorithms that allow a detailed study of the equipment's dynamics at different operating pressures.
- A dynamic random impact model that utilizes the dynamic properties of the peening equipment can be used to predict the induced stresses by needle peening AA2024-T3 sheets.
- Experimental results were able to validate the induced stress predictions.
- The predicted induced stresses can be used as input data of existing forming models to predict the material deflection of Almen-sized AA2024-T3 strips. The results could be improved by taking into account initial rolling stresses.

From the point of view of the equipment characterization, the current state of the equipment is a good starting point for future improvements. Based on its functioning principle, it could be used for applications similar to manual peening and rotary flapper peening. Behaviour anomalies, such as velocity and frequency variations among the needles should be addressed for a better uniformity of the process. By addressing this issue, needle peening would provide surface indentations of the same shape and size; deed difficult to achieve with other manual treatment equipment.

As for the simulation portion of this study, existing models were able to be modified to suit the intricacies of needle peening by using the findings from the equipment characterization as intial boundary conditions. The case of single impact was studied in order to determine the accordance between experimental and predicted indentation diameters for different pressures p. It was determined that the impact model was capable of predicting the plastic deformation

from single impacts, with the exception of the lower end of the studied pressures. The optical determination of the indentation diameters was not capable of distinguishing the material build-up around the affected area. Having this in knowledge, the methodology for the measurement of indentations could be improved. The same model was then modified to simulate multiple, randomly distributed impacts at different pressures. The model was capable of predicting the induced stress profile, proof of this is the close resemblance between the simulated profile and the stress profile determined using the XRD technique for $p = 137.89$ kPa (20 psi) at saturation. The arc-height results provide a good approximation, however these could be improved by accounting for initial forming stresses.

To conclude, the methodology proposed in the frame of this research sets a robust combination of experimental and numerical techniques leveraged to assess the performance and predict the results of needle peening. The set of tools developed during this work can be used to optimize the equipment and to foresee what the design changes would entail. Additionally, the findings made during this project provide the developer with enough information to assess the current state of the prototype. On the other hand this thesis could set the ground for the standardization of the process and for lines of research of other alternative peening technologies. This displays sufficient resources to improve the quality of the tool to better address costumer needs while contributing to the leadership of Quebec in the aerospace industry.

Limitations to the proposed solution and future improvements

The equipment studied was still in development at the time of the experimental campaign. Any variations during its operation were not studied deeply enough to ensure the process runs unaffected during longer time periods of treatment. The analysis is only limited to AA2024-T3 and while it has been proven that different thicknesses can be modeled, that is the only change recommended as far as material goes. Given the budget allocated to the project, only one specimen was tested by XRD. Additional experimental residual stress curves could improve the confidence in the modeling approach.

An FE model that allows for the development of curvatures during the peening process could provide a more realistic approach to the simulation of peening, especially while studying softer materials such as aluminum. The incorporation of different strain amplitudes of the material closer to the surface could improve the prediction of the maximum compressive stresses found in the near-surface. Additionally, a more robust high-speed camera setting could be used to study the deformation of the material upon impact which was not possible with the equipment available for this study.

REFERENCES

Al-Hassani, S. (1999). Numerical simulation of multiple shot impact. In *Proceedings of the 7th International Conference on Shot Peening*, pages 217–227.

Al-Obaid, Y. (1990). Three-dimensional dynamic finite element analysis for shot-peening mechanics. *Computers and Structures*, 36(4):681–689.

Almen, J. and Black, P. (1963). *Residual stresses and fatigue in metals*. McGraw-Hill.

Badreddine, J. (2014). *Modélisation du grenaillage ultrason pour des pièces à géométrie complexe*. PhD thesis, Université de Technologie Troyes.

Baragetti, S. (2001). Three-dimensional finite-element procedures for shot peening residual stress field prediction. *International Journal of Computer Applications in Technology*, 14(1-3):51–63.

Bhuvaraghan, B., Srinivasan, S. M., Maffeo, B., McClain, R. D., Potdar, Y., and Prakash, O. (2010). Shot peening simulation using discrete and finite element methods. *Advances in Engineering Software*, (41):1266–1276.

Cao, W., Fathallah, R., and Castex, L. (1995). Correlation of almen arc height with residual stresses in shot peening process. *Journal of Materials Science and Technology*, 11:967–973.

Cardarelli, F. (2008). *Materials Handbook: A Concise Desktop Reference*. Springer.

Chen, Z., Yang, F., and Meguid, S. A. (2014). Realistic finite element simulations of arc-height development in shot-peened almen strips. *Journal of Engineering Materials and Technology*, 136:7.

ElTobgy and Elbestawi (2004). Three-dimensional elastoplastic finite element model for residual stresses in the shot peening process. *Proceedings of the Insititution of Mechanical Engineers, Part B: Journal of Engineering Manufacture*, 218(11):1471–1481.

Evans, R. (2002). Shot peening process: modelling, verification and optimisation. *Materials science and technology*, 18(8):831–839.

Fathallah, R., Inglebert, G., and Castex, L. (1996). Modelling of shot peening residual stresses and plastic deformation induced in metallic parts. In *Proceedings of the 6th International Shot Peening Conference*.

Forgues, S., Labelle, B., King, M., and Manor, N. (2011). Controlled rotary flap peening for repair applications. In *Proceedings of the 11th International Conference of Shot Peening*.

Forgues, S. and Polanetzki, H. (2014). New peening technology for aerospace applications (turbine engine repairs). In *EI Workshop*, Florida.

Gariépy, A., Larose, L., Perron, C., and Lévesque, M. (2011). Shot peening and peen forming finite element modelling - torwards a quantitative method. *International Journal of Solids and Structures*, (48):2859–2877.

Gariépy, A., Larose, S., Perron, C., Bocher, P., and Lévesque, M. (2013). On the effect of the peening trajectory in shot peen forming. *Finite Elements in Analysis and Design*, 69:48–61.

Gratsy, L. and Andrew, C. (1996). Shot peen forming sheet metal: finite element prediction of deformed shape. *Proceedings of the Insititution of Mechanical Engineers, Part B: Journal of Engineering Manufacture*, 210(4):361–366.

Guagliano, M. (2001). Relating alment intensity to residual stresses induced by shot peening: a numerical approach. *Journal of Materials Processing Technology*, (110):277–286.

Guagliano, M., Vergani, L., Bandini, M., and Gili, F. (1999). An approach to relate the shot peening parameters to the induced residual stresses. In *Proceedings of the 7th International Conference on Shot Peening*, pages 274–282.

Gurova, T., Estefen, S. F., and Leontiev, A. (2012). Efeito de shot peening em peças com tensões pré-existentes de compressão. In *Congresso Nacional de Ensaios Não Destrutivos e Inspeçao XXX*.

Haagensen, P. J. (1998). Introductory fatigue tests on welded joints in high strength steel and aluminium improved by various methods including ultrasonic impact treatment (uit). *International Institute of Welding*.

Han, K., Owen, D. R. J., and Peric, D. (2002). Combined finite/discrete element and explicit/implicit simulations of peen forming process. *Engineering Computations: International Journal for Computer Aided Engineering and Software*, 19(1):92–118.

Han, K. and Peric, D. (2000). A combined finite/discrete element simulation of shot peening processes part i: studies on 2d interaction laws. *Engineering Computations: International Journal for Computer Aided Engineering and Software*, 17(5):593–619.

Hawkinson, E. (1962). Shot peening - history. In *Mechanical Prestressing of Metals*. SAE ISTC Division 20.

Hirai, N., Tosha, K., and Rouhaud, E. (2005). Finite element analysis of shot peening - on the form of a single dent -. In *Proceedings of the 9th International Conference on Fracture*, volume 82-87.

Hong, T., Ooi, J. Y., and Shaw, B. A. (2008). A numerical simulation to relate the shot peening parameters to the induced residual stresses. *Engineering Failure Analysis*, (15):1097–110.

Hribernik, A. and Bombek, G. (2006). Improved method for shot particle velocity measurement within a shotblasting chamber. *Flow Measurement and Instrumentation*, 17(2):99–105.

Karatas, C., Sozen, A., and Dulek, E. (2009). Modelling of residual stresses in the shot peened material c-1020 by artificial neural network. *Expert Systems with Applications*, 36:3514–3521.

Kirk, D. (1996). The development of residual stresses and curvature in mild steel by needle peening. In *Proceedings of the 6th International Shot Peening Conference*.

Klemenz, M., Hochrainer, T., Delonnoy, L., Schulze, V., Vöhringer, O., and Gumbsh, P. (2005). Similarity rules for the shot peening process based on the finite element method. In *Conference proceedings of ICSP9*.

Kobayashi, M., Matusi, T., and Murakami, Y. (1998). Mechanisms of creation of compressive residual stress by shot peening. *International Journal of Fatigue*, 20(5):351–357.

Konitzer, A. and Polanetzki, H. (2011). Implementation of velocity measurement as intensity verification in serial production. In *Proceedings of the 11th International Conference of Shot Peening*, pages 19–24.

Kral, E., Komvopoulos, K., and Bogy, D. (1993). Elastic-plastic finite element analysis of repeated indentation of a half-space by a rigid sphere. *Journal of Applied Mechanics*, 60(4):829–841.

Kudryavtsev, Y., Kleiman, J., Prokopenko, G., Knysh, V., and Gimrede, L. (2004). Effect of ultrasonic peening on microhardness and residual stress in materials and welded elements. In Society for Experimental Mechanics, I., editor, *2004 SEM X International Congress and Exposition on Experimental and Applied Mechanics*.

Levers, A. and Prior, A. (1998). Finite element analysis of shot peening. *Journal of Materials Processing Technology*, 80-81:304–308.

Li, J. K., Mei, Y., Duo, W., and Renzhi, W. (1991). Mechanical approach to the residual stress field induced by shot peening. *Materials Science and Engineering*, 147(2):167–173.

Majzoobi, G. H., Azizi, R., and Nia, A. (2005). A three-dimensional simulation of shot peening process using multiple shot impacts. *Journal of Materials Processing Technology*, (164-165):1226–1234.

Mayuram, M. (2013). Shot peening. In Wang, Q. and Chung, Y.-W., editors, *Encyclopedia of Tribology*, pages 3081–3085. Springer US.

Meguid, S. A., Shagal, G., and Stranart, J. C. (1999). Finite element modelling of shot-peening residual stresses. *Journal of Materials Processing Technology*, 92-93:401–404.

Meo, M. and Vignjevic, R. (2003). Finite element analysis of residual stress induced by shot peening process'. *Advances in Engineering Software*, 34(9):569–575.

Miao, H., Demers, D., Larose, S., Perron, C., and Lévesque, M. (2010). Experimental study of shot peening and stress peen forming. *Journal of Materials Processing Technology*, 210:2089–2102.

Miao, H. Y., Larose, S., Perron, C., and Lévesque, M. (2009). On the potential applications of a 3d random finite element model for the simulation of shot peening. *Advances in Engineering Software*, (40):1023–1038.

Miao, H. Y., Larose, S., Perron, C., and Lévesque, M. (2011). Numerical simulation of the stress peen forming process and experimental validation. *Advances in Engineering Software*, (42):963–975.

Mori, K., Osakada, K., and Matruoka, N. (1994). Finite element analysis of peening process with plasticity deforming shot. *Journal of Materials Processing Technology*, 45(1):607–612.

Mylonas, G. I. and Labeas, G. (2011). Numerical modelling of shot peening process and corresponding products: Residual stress, surface roughness and cold work prediction. *Surface and Coating Technology*, 205(19):4480 4494.

Rouhaud, E. and Deslaef, D. (2002). Influence of shots' material on shot peening, a finite element model. In *Materials science forum*, page 404.

Rouhaud, E., Ouakka, A., Ould, C., Chaboche, J.-L., and Francois, M. (2005). Finite element model of shot peening, effects of constitutive laws of material. In *Conference proceedings of ICSP9*.

Rouquette, S., Houhaud, E., Francois, M., Roos, A., and Chaboche, J.-L. (2009). Coupled thermo-mechanical simulations of shot impacts: Effects of the temperature on the residual stress field due to shot-peening. *Journal of Materials Processing Technology*, 209:3879–3886.

SAE (2010). Procedures for using standard shot peening almen strip.

SAE (2013a). Shot peening coverage determination.

SAE (2013b). Test strip, holder, and gage for shot peening.

Schiffner, S. and Droste, C. (1999). Simulation of residual stresses by shot peening. *Computers and Structures*, (72):329–340.

Schulze, V., Klemenz, M., and Zimmermann, M. (2008). State of the art in shot peening simulation. In *Proceedings of the 10th International Conference on Shot Peening*.

Schwarzer, J., Schulze, V., and Vöhringer, O. (2002). Finite element simulation of shot peening - a method to evaluate the influence of peening parameters on surface characteristics. In *Proceedings of the 8th International Shot Peening Conference*, pages 508–515.

Sharpe, W. (2008). *Springer Handbook of experimental solid mechanics*. Springer Science & Business media.

Shen, S. and Alturi, S. N. (2006). An analytical model for shot peening induced residual stresses. *CMC*, 4(2):75–85.

Tekeli, S. (2002). Enhancement of fatigue strength of sae 9245 steel by shot peening. *Material letters*, 57(3):604–608.

Voyiadjis, G. Z. and Kattan, P. (1983). Indentation of a half-space with a rigid indentor. *International Journal for Numerical Methods in Engineering*, 19:1555–1578.

Wang, S., Li, Y., Yao, M., and Wang, R. (1998). Compressive residual stress introduced by shot peening. *Journal of Materials Processing Technologya*, 73:64–73.

Wang, T., Platts, M. J., and Levers, A. (2006). A process model for shot peen forming. *Journal of Materials Processing Technology*, 172:159–162.

Wohlfahrt, H. (1984). The influence of peening conditions on the resulting distribution of residual stress. In *Proceedings of the Second International Conference of Shot Peening*, pages 316–331.

Zeng, Y. (2002). Finite element simulation of shot peen forming. In Wagner, L., editor, *Proceedings of the 8th International Shot Peening Conference*, volume 554.

Zimmermann, M., Schulze, V., Baron, H. U., and Löhe, D. (2008). A novel 3d finite element simulation model for the prediction of the residual stress state after shot peening. In *Proceedings of the 10th International Conference on Shot Peening*.

Zimmermann, M., Schulze, V., and Hoffmeister, J. (2010). Finite element modelling of coverage effects during shot peening of in718. *International Journal of Materials Research*, 101(8):951–962.

Zion, H. L. and Johnson, W. S. (2006). Parametric two-dimensional finite element investigation: Shot peening of high strength steel. *AIAA Journal*, 44(9):1973–1982.